國立交通大學

電子工程學系　　電子研究所

碩 士 論 文

利用溫度效應實驗分析奈米級超薄介電層場效電晶體之遠距散射機制

Temperature-Dependent Experiment to Distinguish Remote Scatterers in Polysilicon Ultrathin Gate Oxide MOSFETs

研究生: 光心君 Shin-Jiun Kuang

指導教授: 陳明哲 博士 Prof. Ming-Jer Chen

中華民國 一００ 年 八 月

利用溫度效應實驗分析奈米級超薄介電層場效電晶體之遠距散射機制

Temperature-Dependent Experiment to Distinguish Remote Scatterers in Polysilicon Ultrathin Gate Oxide MOSFETs

研究生：光心君 Shin-Jiun Kuang

指導教授：陳明哲 博士 Prof. Ming-Jer Chen

國立交通大學

電子工程學系　電子研究所

碩士論文

A Thesis

Submitted to Department of Electronics Engineering &

Institute of Electronics

College of Electrical and Computer Engineering

National Chiao Tung University

in Partial Fulfillment of the Requirements

for the Degree of

Master of Science

in

Electronics Engineering

August 2011

Hsinchu, Taiwan, Republic of China

中華民國 一００ 年 八 月

利用溫度效應實驗分析奈米級超薄介電層場效電晶體之遠距散射機制

研究生: 光心君　　指導教授: 陳明哲 博士

國立交通大學

電子工程學系 電子研究所碩士班

摘要

由近年研究可得知，元件尺寸縮減時電子遷移率會伴隨遞減，這也指出了有額外的碰撞機制存在，並且此機制會對下一世代的元件造成很大的影響。因此本篇論文主旨係利用實驗萃取額外遷移率之溫度係數，進而探討N型超薄介電層場效電晶體下的遠距離散射機制。研究方法主要藉由一系列有系統的實驗與平面場效電晶體量子模擬器的搭配，由溫度效應去探討近年倍受爭議之遠距離庫倫散射的來源，並分辨造成遷移率大幅下降的主要碰撞機制為表面電漿子或遠距離聲子散射。而研究結果主要有以下兩點：(1). 即使改變表面粗糙度係數，其實驗萃取額外遷移率得到的溫度係數皆為負值，這說明了遠距離庫倫散射的主要來源是多晶矽空乏區中的表面電漿子。(2). 由近年的發表文獻可得知，表面電漿子之溫度係數約為-1.0，遠距離聲子散射的係數為-2.2 左右。而在此實驗萃取額外遷移率得到的溫度係數皆落於-1.0 附近，故我們認為表面電漿子是造成遷移率大幅下降的主要碰撞機制。

Temperature-Dependent Experiment to Distinguish Remote Scatterers in Polysilicon Ultrathin Gate Oxide MOSFETs

Student: Shin-Jiun Kuang Advisor: Dr. Ming-Jer Chen

Department of Electronics Engineering and Institute of Electronics

National Chiao Tung University

Abstract

Electron mobility degradation is currently frequently encountered in highly scaled devices. This means that additional scattering mechanisms exist and will become profoundly important in next generation of devices. The aim of this work is to experimentally distinguish these remote scatterers particularly concerning the controversial arguments over remote Coulomb scatterers (RCS). To clarify whether Coulomb drag or surface optical (SO) phonons mode is responsible for the degraded electron mobility in n^+-polysilicon ultrathin gate oxide nMOSFETs, we apply a novel temperature-dependent experimental method to obtain corresponding mobility component in high effective field regions. The results are remarkable: (i) in a considerable range of surface roughness amplitudes (Δ), the temperature coefficient exhibits a negative value, confirming interface plasmons in poly depletion region to be dominant remote Coulomb scatterers; and (ii) a new criterion is created with which one can experimentally distinguish interface plasmons from SO phonons: if a power-law temperature exponent γ is close to -1.0, additional scattering with interface plasmons dominates, while for scattering with SO phonons, γ lies around -2.2. In this work, we obtained γ whose value remains around -1.0. Hence we reasonably argue that Coulomb drag due to interface plasmons is responsible.

Acknowledgements

能進 309A 實驗室真的是件很幸福的事情。

很感謝陳明哲老師在碩班兩年中不僅開拓了我研究的視野，更是以身教方式讓我學習到對研究的熱情與態度；最重要的是老師總是關心著每個學生，並給了我們一對自由的翅膀在研究的藍天中恣意翱翔。謝謝博士班的李建志、許智育、李韋漢和張立鳴學長，在你們的細心指導與包容下，才能讓實驗室總是充滿著笑聲與歡樂的氣氛。沒有老師與你們，真的就不會有現在的自己。也很謝謝有同屆的張洛豪、彭霖祥與林煜翔的陪伴，讓我總能在遇到問題時回頭就發現我不是一個人在面對。我有一群好貼心的學弟妹們，謝謝你們總是幫我打氣並且在研究中給予大力的協助。另外我要感謝中興電機系的張書通老師與研究室學長姐們，謝謝老師從大學一直以來的關心跟幫忙，才能讓我到現在仍舊覺得研究是件很快樂的事情。最後我要謝謝最愛的家人、杜立博與親愛的好朋友們，你們一直都是我最重要的後盾與城牆，讓我隨時都能躲回你們的懷抱中獲得慰藉。

我是個幸運的人，所以能進到陳明哲老師的實驗室；我也是個幸福的人，才能擁有不只是 Lab 夥伴關係的真感情。能遇到一群相知相惜一起做研究玩樂的朋友，真的是件很快樂灑花的事情！謝謝你們!

2011 年 8 月

光心君

Contents

Figure Captions

Table Captions

Chapter 1

Introduction

It is well known that the inversion layer mobility of nMOSFETs can be limited to three primary scattering mechanisms: (1). The Coulomb impurity scattering due to the ionized impurity atoms in substrate depletion region; (2). The acoustic/optical phonon scattering in inversion channel region; and (3). The surface roughness scattering at SiO_2/Si substrate interface. However, owing to the measured effective mobility that drops off in highly scaled devices, additional scattering mechanisms exist. So far, in the open literature dedicated to long-channel nMOSFETs with polysilicon ultrathin gate oxides, origins of mobility degradation remained controversial. Additional scatterers can be generalized in terms of the remote surface roughness, source/drain (S/D) plasmons, fixed oxide charge, remote Coulomb scattering, and remote phonon scattering due to surface optical (SO) phonons. First term can be removed because F. Ga´miz,*et al*. [1] have verified by the Monte Carlo simulation that the remote surface roughness-limited mobility increases as the inversion sheet density increases. Hence the effect on the measured effective mobility is insignificant in high vertical electric field region. Second, while channel length is shrinking into the region within Thomas-Fermi screening length (like sub-40 nm device), electron interactions occur near highly doping source/drain (S/D) and channel interface can be viewed as the dynamic screening, resulting in the excitation plasmons emission and/or absorption and then transferring the momentum to affect the current indirectly, according to the published simulation results [2]. Nevertheless, S/D plasmons can be ignored in long channel devices we used in this work. Third, the effect of fixed surface oxide charge revealed similar trends like remote surface

roughness mechanisms [3].

Excluding the remote scatterers mentioned above, it is essential to reconfirm the origin of main remote scatterers to distinguish between remote Coulomb scattering and SO phonons. We discussed the issue prior to remote Coulomb scattering which was thought to have two possible sources. The first source stems from ionized impurity atoms in polysilicon depletion region by Krishnan [4]. However, Yang *et al.*[5] examined remote Coulomb scattering because of space charge in poly side, and their simulated results have shown that it is not the primary role in mobility degradation. On the contrary, series of study by Fischetti and co-workers [6]-[8] pointed out that the free electron counterparts can give rise to interface plasmons near polysilicon and SiO_2 interface which is responsible for mobility degradation when high vertical effective electric field region. This is the second source also named Coulomb drag.

Moreover, we have to further deal with the main source of degraded mobility. Although scattering by SO phonons mode is considered to be dominant in high-k dielectrics [8], its significance relative to Coulomb drag in ultrathin SiO2 gate oxide stacks was controversial in the open literature [8], [9]. From Figure 7 and Figure 8 in Ref. [8], these figures have disclosed that the decay rate of mobility with sheet density due to interface plasmons is larger than the rate by SO phonons, hence illustrating that Coulomb drag plays a major role at high inversion charge densities ($N_{inv}>1\times10^{13}cm^{-2}$). In Ref.[9], by using inverse modeling, they extracted additional mobility and claimed that SO phonon mode is more severe in high-k dielectric than SiO_2 stacks, but they didn't take Coulomb drag in poly side into account.

In order to clarify the discordant argument on remote scatterers, here we elaborated on a novel temperature-oriented experimental method dedicated to

polysilicon ultrathin gate oxide case. The flowchart of the method is shown in Figure 1.1. The proposed method in this work consists of three steps: First, we calculated the temperature-dependent effective mobility which combines the simulated universal curve and Coulomb impurity-limited mobility according to Matthiessen's rule. Consequently, experimentally assessed additional scattering by remote scatterers would be extracted straightforwardly. For the first time, the temperature-oriented additional mobility is obtained; it can lead us to clarify the possible major role in remote scatterers. Second, we also quoted the detailed model for calculating remote coulomb scattering due to ionized impurity atoms in poly depletion region to compare with the experimental additional mobility in this work. Last but not least, a new criterion with a power-law temperature relationship of $\mu_{add} \propto T^{\gamma}$ is created with which one can experimentally distinguish interface plasmons from SO phonons: Based on references [6] and [7], if a power-law temperature exponent γ stays around -1.0, additional scattering with interface plasmons dominates[6]; on the contrary, while for scattering with SO phonons [7], γ is close to -2.2. These results are established on the condition of high measurement temperatures. In addition, validity of Matthiessen's rule used in this work is addressed as well.

Chapter 2

Physical Theory and Electron Mobility Model

2.1 Physical Theory

2.1.1 Schrődinger and Poisson Self-consistent "NEP" in n-MOSFETs

This section will introduce the fully Schrődinger and Poisson self-consistent solver in n-channel MOSFETs, particularly our established simulator **"NEP"** [10]. The schematic of energy band diagram is given in Figure 2.1. We separated the band diagram of silicon substrate along out-of-plane direction into two parts: one is the surface quantum confinement region ($W_{quantum} = 30\ nm$) and other is the bulk classical region ($W_{classical}$) which is defined as

$$W_{classical} = W_{dep} + 1.5 \times W_{quantum} \tag{2.1}$$

where W_{dep} is the space charge width according to abrupt depletion approximation. In the former region, the carriers are confined in this thin region with 300 mesh intervals of width $dz_0 = 0.1$ nm to ensure simulation accuracy. In the latter region, we adopt the conventional formula to handle and it is divided into 50 intervals with a width of $dz_1 = \frac{(W_{dep} + 45)}{50}$ nm. It can significantly reduce the computational time but not losing the accuracy. Moreover, the conduction band edge at the interface is set to be zero of energy in n-MOSFETs.

Figure 2.2 illustrates the common self-consistent steps along with the flow-chart. First, we guessed the surface band bending V_s in Poisson equation by $V_{(z=0)} = V_s$ and $V_{(z=bulk)} = 0$ for the boundary conditions. It would obtain the corresponding initial

potential profile $V(z)$ and hence we can begin with the calculations of 1D Schrődinger equation along with $V(z)$ via the formula

$$-\frac{\hbar^2}{2m}\nabla^2\Psi + V\Psi = E\Psi \tag{2.2}$$

According to Eq. (2.2), the Schrödinger equation can also be written as a general differential equation by the finite element method:

$$-\frac{\hbar^2}{2m}[\frac{\Psi(x_{i-1})-2\Psi(x_i)+\Psi(x_{i+1})}{\Delta x^2}]+V(x_i)\Psi(x_i)=E\Psi(x_i) \tag{2.3}$$

$$\Psi=\sum_n a_n\psi_n \tag{2.4}$$

where E is an eigen-value which has n values, and it is also assumed that the wave-function Ψ is confined in a small region of $\boldsymbol{W_q}$ which includes the entire inversion region completely. In general, the wave-function Ψ dividing this region into n intervals of the equal-distance $\Delta x = W_q / n$ can be expanded in terms of an orthogonal basis set $\{\psi_n\}$. Finally, we apply Newton's method to solve the self-consistent Poisson and Schrődinger equations. The simulated results include n eigen-values (E_n) corresponding to the n wave-function (ψ_n). The smallest eigen-value is defined as the ground state, with the others as the excited states.

. By previous paragraph mentioned, we would get the eigen-values and the wave-function. Besides, we summarize the basic formulation and the iteration that we use to perform a self-consistent solution. In the surface quantum confinement region, the three-dimensional carriers (both electrons and holes) density can be described by

$$n_{3D}(z)=\sum_{i,j}\int_{E_{i,j}}^{\infty} DOS_{i,j}(E)_{2D}f(E)dE\cdot\left|\Psi_{i,j}(z)\right|^2$$

$$=\sum_{i,j} g_i\frac{m^i_{DOS}}{\pi\hbar^2}k_BT\ln\left(1+\mathrm{e}^{(\frac{E_f-E_{i,j}}{kT})}\right)\cdot\left|\Psi_{i,j}(z)\right|^2 \tag{2.5}$$

$$p_{3D}(z)=\sum_{k,j}\int_{-\infty}^{E_{k,j}} DOS_{k,j}(E)_{2D}(1-f(E))dE\cdot\left|\Psi_{k,j}(z)\right|^2$$

$$=\sum_{k,j} g_k \frac{m_{DOS}^k}{\pi\hbar^2} k_B T \ln\left(1+e^{(\frac{E_{k,j}-E_f}{kT})}\right)\cdot\left|\Psi_{k,j}(z)\right|^2 \quad (2.6)$$

where i and k are the electron valley index and the hole valley index, respectively. j is the subband index, and g_i and g_k are the degeneracy of the ith valley and kth type, respectively; m_{DOS}^i and m_{DOS}^k are the density of states electron and hole effective mass, and $E_{i,j}$ and $E_{k,j}$ are the electron and hole energy levels. The corresponding wave-functions $\Psi_{i,j}$ and $\Psi_{k,j}$ are all normalized. In the bulk classical region, the carrier density is given by:

$$n(z)=n_0\cdot\exp(\frac{V(z)}{k_B T}) \quad (2.7)$$

$$p(z)=p_0\cdot\exp(\frac{-V(z)}{k_B T}) \quad (2.8)$$

where p_0 and n_0 are the carrier concentration under the thermal equilibrium. Substituting the above concentration into the 1D Poisson equation, the formula is given by

$$\frac{d^2V(z)}{dz}=-\frac{-q_0\cdot[-N_d^+(z)-n(z)+p(z)]}{\varepsilon_{si}} \quad (2.9)$$

where $N_d^+(z)$ is the ionized donor density. Eventually, we can obtain a new potential $V(z)$ to satisfy with Eq. (2.9) and continuously iterate the procedure by Newton's method until the potential profile $V(z)$ is equal for successive iterations, within a tolerable error range. The two-dimensional electron density can be written as

$$n_{i,j}=g_i\frac{m_{DOS}^i}{\pi\hbar^2}k_B T\ln\left(1+e^{\frac{E_f-E_{i,j}}{kT}}\right) \quad (2.10)$$

The total inversion layer charge density is shown below

$$N_{inv} = \sum_{i,j} n_{i,j} \,. \tag{2.11}$$

and the average inversion layer thickness Z_{av} is described as

$$Z_{av} = \sum_{i,j} \left[\frac{n_{i,j}}{N_s} \cdot \int_0^{bulk} z \cdot \left| \Psi_{i,j}(z) \right|^2 dz \right]. \tag{2.12}$$

We demonstrated the potential calculation for the high doping poly-silicon gate situation:

$$V_{fb} = -k_B T \ln\left(\frac{N_{ploy} N_{sub}}{n_i^2}\right) \tag{2.13}$$

where V_{fb} is the flat band voltage, N_{poly} and N_{sub} are the poly gate concentration and the substrate doping concentration, n_i is the intrinsic concentration and k_B is the Boltzmann's constant.

The method to calculate poly gate voltage is similar with the potential on substrate region. Based on the electrostatics boundary conditions and abrupt depletion approximation, the following formula are given as

$$\varepsilon_{si} E_{si,\max} = \varepsilon_{ox} E_{ox} = \varepsilon_{si} E_{poly,\max} \rightarrow E_{si,\max} = E_{poly,\max} = \frac{Q_{inv} + Q_{dep}(C/cm^2)}{\varepsilon_{si}} \tag{2. 14}$$

$$V_{poly\_abrupt}(x) = \frac{-qN_D\left(\frac{1}{2}x^2 + \left(W_{dep\_abrupt}\right)x\right)}{\varepsilon_{si}} \tag{2.15}$$

$$V_{poly\_drop} = \max\left(V_{poly}(x)\right) - \min\left(V_{poly}(x)\right), \quad -W_{dep\_abrupt} < x < 0 \tag{2. 16}$$

Therefore, using the classical concentration and Poisson equation self consistent method to converge the correct polygate voltage and extract some important results, such as the space charge density and free electron concentration in poly side by the $V_0(start) = V_{poly\_drop}$ and $V_0(end) = 0$ for the boundary condition. Besides,oxide

voltage is written as:

$$V_{ox} = \frac{t_{ox}\varepsilon_{Si}F_s}{\varepsilon_{ox}} \tag{2.17}$$

where t_{ox} is the oxide thickness, ε_{si} and ε_{ox} are the dielectric constant of the silicon and oxide, respectively, and the surface electric field is given by $F_s = \frac{V_{(z=1)} - V_{(z=2)}}{\Delta z}$. Eventually, the total gate voltage can be expressed as

$$V_g = V_s + V_{ox} + V_{poly} + V_{fb} \tag{2.18}$$

where V_s indicates the surface band bending determined by the potential profile in the silicon substrate.

2.2 Electron Mobility Model

Introduction

In this section, we divided it into three parts: First, we calculated the universal electron mobility under the relaxation time approximation which uses the sub-band energy and the wave function provided by our NEP simulator. We consider only lowest four subbands in twofold valleys and two subbands in fourfold valleys to obtain corresponding mobility. Besides, we discussed the momentum relation rates caused by scattering with phonons and surface roughness which can be considered as the expression of universal curve. Second, we quoted a physically based Coulomb-limited mobility model with ionized impurities in substrate by Hauser *et al.* [12]. Consequently, the thick oxide effective electron mobility can be treated as the combination of the universal electron mobility and Coulomb-limited mobility according to Matthiessen's rule. Validity of Matthiessen's rule will be addressed in Chap.4 as well. Third, we also quoted the detailed model by Yang *et al.* [5] to calculate remote-Coulomb-limited mobility due to ionized impurity atoms in depletion region of n-type polysilicon gate (n-polygate) to compare with experimentally additional mobility in this work.

Figure 2.3 illustrates that the calculated universal electron mobility is insensitive to substrate concentrations or process parameters, especially when plotted as a function of high effective field (E_{eff}). E_{eff} can be defined empirically as in the following formula

$$E_{eff} = \frac{q_0 \cdot (\eta N_{inv} + N_{dep})}{\varepsilon_{si} \cdot \varepsilon_0} \tag{2.19}$$

where η is taken to 0.5, inversion carrier concentration(N_{inv}) and the surface

concentration of the depletion charge(N_{dep}) are determined by NEP. Finally, all of the scattering parameters used in this work are listed on Table I.

2.2.1 Phonon Scattering Mechanism and Model

It is well known that the pressure waves which result from the lattice vibrations would deform the crystal deformational potential, perturbing the dipole moment between atoms and giving rise to degradation of inversion layer mobility. The phonon scattering mechanisms are classified into two types, one is acoustic phonon scattering which displaces adjacent atoms in the same directions and the other is optical phonon scattering which displaces neighboring atoms in opposite directions. According to the phase of the vibration with the two different atoms in one primitive cell, acoustic phonon energy is smaller than carrier energy. The energy of the k_{th} intervalley f-*type* phonon $E_{k(f)}$ is 59 meV, and the energy of the k_{th} intervalley g-*type* phonon $E_{k(g)}$ is 63meV. Intravalley phonon scattering only considers acoustic phonons but is forbidden for optical phonons. Hence according to Takagi, *et al.* [13], the momentum-relaxation rate $\tau_{ac}^{u,v}(E)$ from the u_{th} subband to the v_{th} subband is written as:

$$\frac{1}{\tau_{ac(2/4)}^{u,v}} = \frac{n_{v(2/4)}^{ac} m_{d(2/4)} \left(D_{ac}\right)^2 k_B T}{\hbar^3 \rho \left(s_l\right)^2} \frac{1}{Z_{u,v}}, Z_{u,v} = \left(\int \varphi_u^2(z) \varphi_v^2(z) dz\right)^{-1} \tag{2.20}$$

where the index of (2/4) in $\tau_{ac(2/4)}^{u,v}$ represents twofold and fourfold valleys, respectively, D_{ac} (=12 eV) denotes the deformation potential due to acoustic phonons, n_{v2}^{ac} (=2)and n_{v4}^{ac} (=1) are the degeneracy of the twofold valleys and fourfold valleys for intravalley scattering, respectively. ρ is the crystal density, s_l is the sound

velocity, $Z_{u,v}$ is the form factor combined with the wavefunctions of the u-th subband and the v-th subbands, $\hbar$ is the Planck constant divided by 2π, and k_B is the Boltzmann constant. The total scattering rate in u_{th} subband is determined by summing up $\tau_{ac}^{u,v}$ within all the subbands, and it can be given as

$$\frac{1}{\tau_{ac(2/4)}^{u}(E)} = \sum_{v} \frac{U(E-E_u)}{\tau_{ac(2/4)}^{u,v}(E)} \tag{2.21}$$

where $U(x)$ is a step function for $U(x) = 1(x \geq 0),\ 0(x < 0)$.

Considering the intervalley phonon scattering model, the $\tau_{INTER}^{u,v}(E)$ from u_{th} subband in twofold valleys to the v_{th} subband in fourfold subband can be described as

$$\frac{1}{\tau_{INTER2}^{u,v}(E)} = \sum_{k}^{\{f\}} \frac{n_{v2\to4}^{f} m_{d4} (D_k)^2}{2\hbar\rho E_k} \frac{1}{W_{u,v}^{'}} \left(N_k + \frac{1}{2} \pm \frac{1}{2} \right) \times \frac{1 - f(E \mp E_k)}{1 - f(E)} \times U(E \mp E_k - E_v) \tag{2.22}$$

$$W_{u,v}^{'} = \left(\int \varphi_u^2(z) \varphi_v^{'2}(z) dz \right)^{-1} \tag{2.23}$$

where $n_{v2\to4}^{f}$ (=4) denotes the degeneracy of the valleys about intervalley scattering, E_k and D_k are the deformation energy and potential with respect to the k_{th} intervalley phonon, as well as m_{d4} is the density-of-states effective mass of the final state (fourfold valley). Besides, the signs in $\left(N_k + \frac{1}{2} \pm \frac{1}{2} \right)$ indicates that "+" means phonons emission and " — " means phonons absorption. N_k signifying the occupation number of the k_{th} intervalley phonon is given by

$$N_k = \frac{1}{[\exp(\frac{E_k}{k_B T}) - 1]} \tag{2.24}$$

Similarly, $\tau_{INTER4}^{u,v}{}'(E)$ from u_{th} subband in fourfold valleys to the v_{th} subband in

twofold subband, and $\tau^{u,v}_{INTER4}(E)$ from u_{th} subband in fourfold valleys to the v_{th} subband in fourfold subband, can all be written as

$$\frac{1}{\tau^{u,v}_{INTER4}{}'(E)} = \sum_{k}^{\{f\}} \frac{n^{f}_{v4\to 2} m_{d2} (D_k)^2}{2\hbar\rho E_k} \frac{1}{W_{u,v}} \left(N_k + \frac{1}{2} \pm \frac{1}{2} \right) \times \frac{1 - f(E \mp E_k)}{1 - f(E)} \times U(E \mp E_k - E_v') \quad (2.25)$$

$$W_{u,v} = \left(\int \varphi_u'^{2}(z) \varphi_v^{2}(z) dz \right)^{-1} \quad (2.26)$$

$$\begin{aligned} \frac{1}{\tau^{u,v}_{INTER4}(E)} = & \sum_{k}^{\{f\}} \frac{n^{f}_{v4\to 4} m_{d4} (D_k)^2}{2\hbar\rho E_k} \frac{1}{Z'_{u,v}} \left(N_k + \frac{1}{2} \pm \frac{1}{2} \right) \times \frac{1 - f(E \mp E_k)}{1 - f(E)} \times U(E \mp E_k - E_v') \\ & + \sum_{k}^{\{g\}} \frac{n^{g}_{v4\to 4} m_{d4} (D_k)^2}{2\hbar\rho E_k} \frac{1}{Z'_{u,v}} \left(N_k + \frac{1}{2} \pm \frac{1}{2} \right) \times \frac{1 - f(E \mp E_k)}{1 - f(E)} \times U(E \mp E_k - E_v') \end{aligned} \quad (2.27)$$

where $n^{f}_{v4\to 2}$ (=2), $n^{g}_{v4\to 4}$ (=1), and $n^{f}_{v4\to 4}$ (=2) are the corresponding degeneracy of the intervalley phonon scattering.

2.2.2 Surface Roughness Scattering Mechanism and Model

At high effective field, the roughness scattering at the Si/SiO_2 interface dominates the performance of a MOSFET device, resulting in the mobility degradation in the inversion layer. Analysis of mobility usually involves two kinds of assumptions, one is the Gaussian autocovariance function and the other is exponential autocovariance function. In this work, we prefer use of the Gaussian autocovariance function, because the calculation of surface roughness scattering rate by exponential model needs larger values of the root mean square amplitude Δ to fit experimental assessed mobility than the Gaussian model. Besides, we make an important assumption that the single subband approximation is quite accurate. Since surface roughness is anisotropic scattering, we only consider the intrasubband scattering. Under Yamakawa's surface roughness model [14], the scattering rate for a Gaussian function is given as

$$\frac{1}{\tau_{SR}^{i,j}(E)} = U(E-E_j)\frac{m_{DOS}^{(j)}(E)e^2 E_{eff}^{ij\ 2}\Delta^2\lambda^2}{2\hbar^3}\int_0^{2\pi} e^{\frac{-q^2\lambda^2}{4}}(1-\cos\theta)d\theta \tag{2.28}$$

Assuming the elastic collisions without energy transition,

$$\frac{1}{\tau_{SR}^{i,j}(E)} = U(E-E_j)\frac{m_{DOS}^{(j)}(E)e^2 E_{eff}^{ij\ 2}\Delta^2\lambda^2}{2\hbar^3}\int_0^{2\pi} \sin^2\frac{\theta}{2}e^{-\frac{m(E-E_j)}{\hbar^2}(1-\cos\theta)\lambda^2}d\theta \tag{2.29}$$

$$q^2 = 2k^2(1-\cos\theta) \tag{2.30}$$

$$k^2 = \frac{2m_{DOS}^{(j)}\cdot(\mathrm{E}\text{-}\mathrm{E}_j)}{\hbar^2} \tag{2.31}$$

where $m_{DOS}^{(j)}$ and $\mathrm{E_j}$ are the density of states effective mass and the electron subband energy in the j_{th} subband. Besides, the new definition of E_{eff}^{ij} can follow Ref. [14] replaces with the empirical formula Eq. (2.19) to obtain more accurate universal curves. The comparison results are depicted in Figure 2.4. The new definition of E_{eff}^{ij} is written as .

$$E_{eff}^{ij} = \int_0^{\infty}\varphi^j(z)\frac{dV}{dz}\varphi^i(z)dz \tag{2.32}$$

where $\varphi^i(z)$ and $\varphi^j(z)$ are the wavefunctions of the initial and final states of the electrons, respectively, and E_{eff}^{ij} is the electron effective field from the i_{th} subband to the j_{th} subband. When the relationship of E-K displayed a parabolic curve, the Eq. (2.17) and Eq. (2.32) would be the same definition.

2.2.3 Derivation of Two-Dimensional Mobility

The scattering rates of the twofold and fourfold valley can be expressed in terms of the phonon scattering and surface roughness scattering for i_{th} subband with the energy (E); hence the equations are described as [13]:

$$\frac{1}{\tau_2^i(E)} = < \frac{1}{\tau_{phonon\_twofold}^i(E)} + \frac{1}{\tau_{SR\_twofold}^i(E)} > \tag{2.33}$$

$$\frac{1}{\tau_4^i(E)} = < \frac{1}{\tau_{phonon\_fourfold}^i(E)} + \frac{1}{\tau_{SR\_fourfold}^i(E)} > \tag{2.34}$$

where $\tau_{phonon\_twofold}^i(E)$ and $\tau_{phonon\_fourfold}^i(E)$ consist of intravalley and intervalley phonon scattering for i_{th} subband of two- and fourfold valleys. Therefore, using the average energy within the 2DEG under the relaxation time approximation, the mobility μ_2^i and μ_4^i for electron in i_{th} subband of two- and fourfold valleys cab be defined as

$$\mu_2^i = \frac{q_o \int_{E_i}^{\infty} (E - E_i)\tau_2^i(E)(-\frac{\partial f}{\partial E})dE}{m_{c2} \int_{E_i}^{\infty} (E - E_i)(-\frac{\partial f}{\partial E})dE} \tag{2.35}$$

$$\mu_4^i = \frac{q_o \int_{E_i^{'}}^{\infty} (E - E_i^{'})\tau_4^i(E)(-\frac{\partial f}{\partial E})dE}{m_{c4} \int_{E_i}^{\infty} (E - E_i^{'})(-\frac{\partial f}{\partial E})dE} \tag{2.36}$$

Consequently, the total universal mobility μ_{uni} averaged over the subband occupation is written as

$$\mu_{uni} = \frac{(\sum_i \mu_2^i N_i + \sum_{i'} \mu_4^{i'} N_{i'})}{N_s} \tag{2.37}$$

2.2.4 Coulomb-Limited Mobility Model due to Ionized Impurity Atoms in the Substrate Region

Coulomb scattering due to ionized impurity atoms in the substrate region causes the degradation of mobility at lower effective field. Because the momentum related rates caused by Coulomb scattering was not established completely yet in NEP

simulator, hence we quoted a physically based Coulomb-limited mobility model by Hauser *et al.* [12]. It is a semi-empirical equation that various components have been modified to obtain best fitting with measured results. The corresponding mobility of Coulomb scattering can be presented by

$$\mu_{C\_impurity} = \frac{1.1\times10^{21}T_n^{1.5}}{\ln(1+\gamma_{BH}^2)-\frac{\gamma_{BH}^2}{1+\gamma_{BH}^2}}\frac{1}{N_{sub}} \tag{2.38}$$

$$\gamma_{BH}^2 = \frac{2\times10^{19}}{\frac{N_{inv}}{z}}T_n^2 \tag{2.39}$$

$$T_n = \frac{T}{300K} \tag{2.40}$$

where γ_{BH} denotes the Brooks-Herring equation, and T_n indicates the normalized temperature. Besides, the inversion charge density (N_{inv}) are calculated from NEP simulator.

Therefore, the calculated thick oxide effective electron mobility excluding the influence on remote-scattering mechanisms can be treated as the combination of the universal electron mobility and Coulomb-limited mobility according to Matthiessen's rule as follows:

$$\frac{1}{\mu_{thick\_oxide}} = \frac{1}{\mu_{c\_impurity}} + \frac{1}{\mu_{uni}} \tag{2.41}$$

2.2.5 Remote Coulomb Scattering Model due to Ionized Impurity Atoms in Polygate Depletion Region

In order to clarify the origin of remote Coulomb scatterers in polygate depletion region, we refer to the momentum remote Coulomb scattering rate due to ionized impurity atoms in poly side [5] for comparison with the experimentally assessed

additional mobility in this work. This model only considered the lowest subband in twofold valley.

The detailed descriptions for two-dimensional (2D) electron density ($n_{i,j}$), total inversion layer charge density (N_{inv}), and the average inversion layer thickness (Z_{av}) have been mentioned in Section.2.2.1. By using a triangular potential approximation and a variation approach, the lowest energy level (E_{11}) and corresponding average inversion layer thickness (Z_{11}) can be written as

$$E_{11} = 1.96556\left(\frac{e^2\hbar}{(m_{1||})^{0.5}\varepsilon_{si}}\right)^{\frac{2}{3}} \cdot \left(N_{dep} + \frac{55}{96}N_{inv}\right)\left(N_{dep} + \frac{11}{32}N_{inv}\right)^{\frac{-1}{3}} \tag{2.42}$$

$$Z_{11} = \left(\frac{9\varepsilon_{si}\hbar^2}{4m_{1||}e^2\left(N_{dep} + \frac{11}{32}N_{inv}\right)}\right)^{\frac{1}{3}} \tag{2.43}$$

where $m_{1||}$ (=0.916×m_o) is normal electron effective mass, and the space charge for depletion region (N_{dep}) is given by

$$N_{dep} = \sqrt{\frac{2\varepsilon_{si}\varphi_d N_{sub}}{e}} \tag{2.44}$$

where φ_d is the surface band bending in substrate region, and is described by

$$\varphi_d = \frac{E_F + E_{F,bulk} - k_B T}{e} - \frac{eN_{inv}Z_{av}}{\varepsilon_{si}},\ E_{F,bulk} = E_g + k_B T \log\left(\frac{N_{sub}}{N_v}\right) \tag{2.45}$$

$E_{F,bulk}$ is the bulk Fermi energy in the substrate region.

The previous results are used for the calculation of remote Coulomb scattering (RCS) due to impurity atoms in polysilicon depletion region. Thus, the corresponding RCS rate at scattering angle θ is given by

$$\frac{1}{\tau(\theta)} = \frac{2\pi e^2 m_{c2}}{\hbar^3} N_{poly} \left|A(S,z)\right|^2 dz \tag{2.46}$$

where m_{c2} (=0.19×m_o) is electron conductivity effective mass, and $\left|A(S,z)\right|^2$ contains the screening effect of inversion layer carrier on impurity atoms in

polysilicon depletion region. The detailed process has been solved in [5], and the result is written as

$$A(S,z)=\frac{eB_o e^{Sz}}{4\pi\bar{\varepsilon}_r D} \tag{2.47}$$

The parameters in Eq.(2.44) are shown below

$$D=S+\bar{s}B_{av}+\bar{s}\frac{(\varepsilon_{si}-\varepsilon_{ox})}{(\varepsilon_{si}+\varepsilon_{ox})}B_0{}^2$$

$$B_0=\frac{b^3}{(b+S)^3}$$

$$B_{av}=(8b^3+9Sb^2+3S^2b)$$

$$b=\frac{3}{Z_{11}}$$

$$\bar{s}=\frac{e^2 N_{inv}}{(\varepsilon_o(\varepsilon_{si}+\varepsilon_{ox})k_B T(1+e^{\frac{-(E_f-E_{11})}{k_B T}})\ln(1+e^{\frac{E_f-E_{11}}{k_B T}}))}$$

$$z=<w>=0.5\times\frac{(N_{inv}+N_{dep})}{N_{poly}} \tag{2.48}$$

By using Eq.(2.44) – Eq.(2.46) and integrating within the polysilicon depletion region, the momentum RCS rate due to ionized impurity is written as

$$\frac{1}{\tau_{RCS}}=\int_0^{2\pi}\frac{1-\cos(\theta)}{\tau(\theta)}d\theta \tag{2.49}$$

Hence the remote Coulomb-limited mobility due to doping impurity in poly side can be described as

$$\mu_{RCS}=\frac{e}{m_{c2}}\frac{\int_0^{\infty}\tau_{RCS}(E-E_{11})\frac{\partial f_0}{\partial \mathrm{E}}g(E)dE}{\int_0^{\infty}f_0 g(E)dE} \tag{2.50}$$

where $E\ (=E_{11}+\frac{\hbar^2k^2}{2m_2})$ is total energy in the lowest subband, $g(E)\ (=\frac{2\mathrm{m}_2}{\pi\hbar^2})$ denotes density of states in two dimensional electron gas from twofold valley, and f_0

is Fermi-Dirac distribution function. Eventually, the resulting remote Coulomb mobility due to ionized impurity atoms in poly side with oxide thickness as a parameter is presented in Figure 2.5. Agreements are achieved (see Fig. 8 in [5]).

Chapter 3

Experiment Framework

N-channel devices under test were fabricated in a conventional 90-nm manufacturing technology with different channel width (W) and length (L): W/L=10/10 μm for T_{ox}=1.65nm and W/L=1/1 μm for T_{ox}=1.27 nm. Their SiO2 thin films were grown thermally, followed by NO annealing. Experimental C-V characteristics for W/L=10/10μm as depicted in Figure 3.1 were fitted well using a fully Schrödinger and Poisson self-consistent solver in our simulator (NEP) and by Schred [15]. NEP was employed in fitting the C-V data, and the resulting process parameters of the devices are given in Table II. In addition, the same parameter values are also extracted by the available self-consistent Schrődinger and Poisson's equations solver Schred [15].

3.1 The Measurement Method of the Inversion-Layer Experimentally Assessed Effective Mobility

In measurement method, the conventional inversion-layer mobility is usually extracted as

$$\mu(V_g) = \frac{L}{W} \times \frac{I_d(V_g)}{V_d} \times \frac{I}{eN_{inv}(V_g)} \tag{3.1}$$

$$G_d(V_g) = \frac{I_d(V_g)}{V_d} \tag{3.2}$$

where G_d is drain conductance. When I_g is small sufficiently, G_d can be presented by $\frac{I_{ch}}{V_d}$, and the channel current (I_{ch}) should be the same as drain current (I_d) and source

current (I_s). However, while gate oxides are thin enough to encounter direct tunneling current, high gate leakage current would affect the accurate determination of drain conductance (G_d), hence the G_d is difficult to define simply by $\frac{I_s}{V_d}$ or $\frac{I_d}{V_d}$.

By following the experimental work by Takagi, *et al.* [18], we can know that while gate oxide thicknesses are quite thin, the drastically increased gate current (I_g) affects source current (I_s) and drain current (I_d) with the resulting opposite signs. The schematic diagram of current flow in MOSFETs with high gate leakage current is shown in Figure 3.2 where I_s and I_d can be written as

$$I_s = I_{ch} + I_{GS} \tag{3.3}$$

$$I_d = I_{ch} - I_{GD} \tag{3.4}$$

where I_{GS} and I_{GD} are the current from the source to the gate and the current from the drain to gate, besides $Is<0$ and $I_d>0$. Figure 3.2 illustrated that I_s is larger than the current from the source into the channel (I_{ch}) due to the current flows from source to gate(I_{GS}), but I_d is smaller than the current from channel to gate (I_{ch}) because the current tunnels from drain into gate (I_{GD}). When V_d is sufficiently small, the I_{GS} must be the same as the I_{GD} , hence the channel current can be defined as $I_{ch} = \frac{I_d + I_s}{2}$ .Therefore, inversion layer (channel) mobility is measured by

$$\mu(V_g) = \frac{L}{W} \times \frac{(I_s(V_g) + I_d(V_g))}{2V_d} \times \frac{1}{EN_{inv}(V_g)} \tag{3.5}$$

Considering the difference between L_{mask} and L_{eff}, as well as the issue about the parasitic source/ drain resistance (R_{sd}), Eq. (3.5) could be defined more accurate by

$$\mu_{eff} = (\frac{1}{R_{d's'}}) \frac{(L_{mask} - \Delta L)}{eWN_{inv}} \tag{3.6}$$

$$R_{d's'} = \frac{V_{d's'}}{I_{d's'}} = \frac{2V_{ds}}{I_d + I_s} - R_{sd} \tag{3.7}$$

where L_{mask} is the design length on the polysilicon etch mask and $L_{mask} \approx L_{gate}$. The ΔL is the length of the overlap region between gate and diffusion extensions. The measured effective mobility values (μ_{eff}) are demonstrated in Figure 3.3 versus vertical effective field E_{eff} for two different gate oxide thicknesses.

3.2 Extraction of Source/Drain Series Resistance

Although the parasitic resistance in this research could be neglected, the issue of parasitic resistance should still be mentioned in this section in order to apply for short channel issue in the future.

First, a state-of-the-art n-MOSFET was simulated by TCAD[16] in order to restructure the experimental one. Figure 3.4 illustrates the net doping concentration near the drain edge of n-MOSFETs ($L_{mask} = 0.065\mu m$) used in this work. The process parameters used are gate oxide thickness (T_{ox}) =1.27 nm, n^+ polysilicon doping concentration (N_{poly}) =1×10^{20}cm^{-3}, and the p-type substrate (Psub) =4×10^{17}cm^{-3}. The central doping concentration inside the source/ drain extension (SDE) region is higher than 10^{20} cm^{-3}.The detailed doping parameter and profile were determined by fitting the measured I-V curve at T=292 K. In this situation, the method of extracting parasitic source/ drain resistance (R_{sd}) with V_g-dependence can be described by [19]

$$R_{sd} = \frac{V_{sd}}{I_{sd}} - \frac{\Delta\phi_{sd}}{I_{sd}} \tag{3.8}$$

where $V_{sd} = 0.05V$, $\Delta\phi_{sd}$ is the potential-drop ($\phi_{sorce/channel} - \phi_{channel/drain}$) between the source/ drain extension (SDE) and channel surfaces, which was extracted below

the interface 2.5 nm which belongs to inversion region, and I_{sd} was measured by experiment. Eq. (3.8) regards $\frac{V_{sd}}{I_{sd}}$ as total resistance (R_{tot}), and $\frac{\Delta\phi_{sd}}{I_{sd}}$ can be treated as channel resistance (R_{ch}) with V_g-dependence, hence we can extract the series resistance (R_{sd}) by Eq. (3.8) simply. The schematic of electrostatic potential in channel region at Vg=1.0 V for T=292K is also shown in Figure 3.5. Further, we discuss R_{sd} values under various bias conditions in three gate voltages: 0.8, 1.0, and 1.2 V.

The results of extracting R_{sd} value are summarized in Table III. When gate voltage increases, the corresponding parasitic resistance decreases gradually. Regardless of temperatures used, it is found that $R_{sd}=126\Omega$ at V_g=0.8 V, $R_{sd}=106\Omega$ at V_g =1.0 V, and $R_{sd}=99\Omega$ at V_g=1.2V. Finally, the R_{sd} values obtained by using this simulation study are reasonably consistent with the extracted one ($R_{sd}=120\Omega$) shown in [20]. Thus, we selected $R_{sd}=117\Omega$ as process parameter in W/L= 1/1 μm.

Chapter 4

Analysis and Discussion

In this section, the resulting universal mobility for a correlation length of the surface roughness (λ) of 14.9 Å and root mean square height of the surface roughness amplitude (Δ) of 2.6 Å, which are mentioned in section 2.2.3, was found to reproduce experimental data [17] well for two different temperatures (T=242K, 297K). Corresponding comparison is depicted in Figure 4.1. This confirms the validity of the temperature-dependent universal mobility simulation work. Therefore, we can use the fitting parameters as reference. Since different manufacturing procedures or oxide fabrication steps may result in different universal mobility [19], [21], we took various surface roughness amplitude (Δ) into account with the other process parameters kept fixed. With aforementioned process parameters (see Table II) as inputs, the measured effective mobility (μ_{eff}), simulated universal curves (μ_{uni}), and the calculated universal one with no remote scatterers were plotted in Figure 4.2 for T_{ox}=1.65nm and Figure 4.3 for T_{ox}=1.27nm, both as a function of vertical electrical field (E_{eff}) with Δ as a parameter. What deserves to be mentioned is that the simulated mobility curve and calculated one would be smaller than measured data in this work when Δ = 2.6 Å in Figure 4.2(a), which is the same fitting Δ values as compared with Takagi et al.[17]. The explanation is considerable that different oxide fabrication steps correspond to different additional scattering mechanisms. While the gate oxide replaced pure oxide [17] by the SiO2 film following NO annealing as used in this work, the Δ value would decrease [21]. Therefore, Δ = 2.0 Å should be substituted for Δ = 2.6 Å as upper limit of surface roughness amplitude, and due to the improvement in the progress of manufacturing processes, Δ value should be further reduced as expected. Not only

did the published experiment [22] show that the extracted Δ is 1.2 Å, but also the fitting range of Δ in Fischetti [6], which will be addressed in Section4.2, yielded possible Δ range of 0.8 Å- 2Å.

4.1 The Origin of Remote Coulomb Scattering Mechanism

While comparing measured effective electron mobility (μ_{eff}), the additional scattering by remote scatterers in polysilicon region can be defined by using Matthiessen's rule as follows:

$$\frac{1}{\mu_{\text{eff}}} = \frac{1}{\mu_{thick\_oxide}} + \frac{1}{\mu_{add}} \tag{4.1}$$

the resulting additional mobilities with Δ as a parameter in W/L=10/10 μm and W/L=1/1 μm are depicted in Figure 4.4 and Figure 4.5. These figures illustrate that no matter what Δ values change, the additional scattering becomes more insignificant with decreasing temperature in universal mobility dominant region (E_{eff}>0.7 MV/cm). The results confirm that although we do not know the accurate Δ value in the measured samples, the simulated results all lead to one argument that the origin of remote Coulomb scattering is due to interface plasmons. The reasons are given below.

First, the conventional concept believes that a positive temperature coefficient is expected to be treated as ionized impurity atoms in polysilicon depletion region, but owing to Thomas-Fermi theory of screening effect, the higher temperature would enhance the exponential damping factor and result in the decreased screening effect, the actual trend for case of ionized impurity atoms is not so simple. In order to deal with this unknown situation, we quoted the detailed formula to calculate the remote Coulomb-limited mobility due to ionized impurity atoms in poly side as have been mentioned in Section 2.2.5. The resulting simulations are also shown in Figure 4.4 and Figure 4.5. The results point out that the calculated remote Coulomb-limited

mobility due to ionized impurity atoms is about two orders of magnitude larger than the experimentally assessed additional mobility.

Second, we also produced the formula of temperature-coefficient (η) to clarify the temperature-oriented trend:

$$\eta = \frac{\mu_{add(233K)} - \mu_{add(298K)}}{233K - 298K} \tag{4.2}$$

We can find that the temperature coefficient due to ionized impurity atoms in poly side also displays large inconsistency in comparison with experimentally additional one in this work; the results are depicted in Figure 4.6.

The extra evidence suggests that remote Coulomb scattering dominates over interface plasmons as shown in Figure 4.7 and Figure 4.8. These figures showed that the published [5],[6],[18],[23] degraded mobility values at near-room temperature can be compared with experimentally assessed additional mobility in this work at T=298K. We can find that these additional mobilities from different processes [5],[6],[18],[23] are all close to our additional mobility. Besides, the remote Coulomb-limited mobility due to ionized impurity atoms in poly side is again larger than the published values [5],[6],[18],[23].

Summing up the previous contentions and the trend of additional mobility for increasing temperature which can enhance the absorption and emission of interface plasmons, we assume that interface plasmons dominate remote Coulomb scattering.

4.2 The Main Source of Mobility Degradation in Polysilicon Ultrathin Gate Oxide nMOSFETs Stacks

In this section, we have to further clarify the main source which results in mobility degradation in polygate stacks. This concerns the degraded mobility due to

the surface roughness scattering mechanisms at the SiO_2/Si substrate interface in high E_{eff} region. To alleviate this hurdle, we used the calculated mobility curves to replicate the experimental data for different temperatures simultaneously with Δ as a parameter, the fitting results are shown in Figure 4.9. These figures all point out obviously that none of the single Δ can lead to concurrent reproduction of the measured one with different temperatures in universal dominated region; hence the remote scatterers do exist in this work.

Figure 4.10 illustrates that additional mobility exhibits an increasing trend in low E_{eff} region or low inversion-layer sheet density (N_{inv}) while decreasing gradually for higher E_{eff} (N_{inv} >5×10^{12}cm^{-2}). The increasing trend of additional mobility with E_{eff} can be ascribed to fixed oxide charge density near SiO_2/Si interface. The effect of fixed oxide charge becomes insignificant with increasing N_{inv} due to screening effects, and owing to decreasing screening effect with temperature, additional mobility curve at T=380K is lower than T=292K [3]. Nevertheless, in view of the applicability of Matthiessen's rule, we only considered the high E_{eff} region in this work. In this situation, the effect of fixed oxide charge can be suppressed.

Figure 4.11 has shown the measured data, simulated curves, and the temperature-oriented additional mobility at N_{inv} =1×10^{13}cm^{-2}, along with the power-law relation of $\mu_{add} \propto T^{\gamma}$. The resulting power-law exponent γ versus E_{eff} is depicted in Figure 4.12. The figure reveals obviously that the γ values are all around -1.0, no matter what E_{eff} and Δ was adjusted.

The extra evidence is given blow. First, the simulated interface plasmons limited mobility with 1-nm gate oxide [6] in Figure 4.12 shows that the fitting γ in the same temperature region in this work is close to ours. Second, our additional mobility value is qualitatively similar with the experimentally extracted mobility [9], although we

cannot identify the dominated mechanisms in terms of interface plasmons in the work by Chau, *et al.*[9], unless we can extract the γ value to meet each other. The confirmative evidence supports that the interface plasmons are more dominant than SO phonon mode as the inversion charge density increases, as plotted in Figure 7,8 in Ref.[8]. Similar trends can be found in Figure 4.10.

Therefore, we reach the argument that Coulomb drag due to interface plasmons is the main source for degraded mobility in poly gate oxide stacks.

4.3 The Validity of Matthiessen's rule

Finally, we want to highlight that the validity of Matthiessen's rule in this work is adequate. Therefore, we calculated the universal mobility and the corresponding error using two different microscopic definitions:

$$\frac{1}{\mu^i_{uni}(E)} = < \frac{1}{\mu^i_{phonon}(E)} + \frac{1}{\mu^i_{SR}(E)} > \tag{4.3}$$

$$\frac{1}{\mu^i_{uni}(E)} = < \frac{1}{\mu^i_{phonon}(E)} > + < \frac{1}{\mu^i_{SR}(E)} > \quad according\ to\ Matthiessen's\ rule \tag{4.4}$$

The comparison results with temperatures as a parameter are shown in Figure 4.13. Obviously, although using Matthiessen's rule would overestimate the value of universal mobility, the maximum error of universal mobility caused by using Matthiessen's rule is below 5%. Thus, this error is insignificant as compared with the measured or simulated effective mobility difference (see Figure 4.2 and Figure 4.3). Importantly, high vertical effective electric field is involved only. Thus, the validity of Matthiessen's rule used in this work is adequate.

Chapter 5

Conclusion

In this work, we have experimentally established a novel temperature-dependent method to obtain additional electron mobility due to remote scatterers and its power-law temperature exponent in ultrathin gate oxide polysilicon nMOSFETs operated at high vertical effective field.

First, in a considerable range of surface roughness amplitudes (Δ), the resulting additional mobility component for mobility degradation for the first time exhibits a negative temperature coefficient (η). We also quoted the detailed formula to calculate the remote Coulomb-limited mobility due to ionized impurity atoms in polygate depletion region. The simulated result is about two orders of magnitude larger than experimentally additional mobility in this work. The temperature coefficient (η) due to impurity atoms in poly side also exhibits a large discrepancy as compared with experimental additional one. Second, the temperature exponent (γ) extracted from experimentally additional mobility points out that the interface plasmon mode is more significant than SO phonons in this work, as supported by the existing sophisticated simulation[8].

Therefore, we reasonably confirm that Coulomb drag due to interface plasmons to be the dominant remote Coulomb scatterers and the main source of degraded mobility in ultrathin gate oxide polysilicon stacks. In addition, validity of Matthiessen's rule used in this work has been verified .

References

[1]. F. Gámiz and J. B. Roldan, “Scattering of electrons in silicon inversion layers by remote surface roughness,” *J. Appl. Phys.*, vol. **94**, no. 1, pp. 392-399, July 2003.

[2]. M. V. Fischetti , S. Jin , T.-W. Tang , P. Asbeck , Y. Taur , S. E. Laux , M. Rodwell and N. Sano, "Scaling MOSFETs to 10 nm: Coulomb effects, source starvation, and virtual source model", *J. Comput. Electron.*, vol. **8**, p.60 , 2009.

[3]. T. H. Ning and C. T. Sah, “Effects of inhomogeneities of surface-oxide charges on the electron energy levels in a semiconductor surface-inversion layer,” *Physical Review B*, vol. **9**, pp. 527-535, Jan.1974

[4]. M. S. Krishnan, Y. C. Yeo, Q. Lu, T. J. King, J. Bokor, and C. Hu, “Remote charge scattering in MOSFETs with ultra-thin gate dielectrics,” in *IEDM Tech. Dig.*, 1998, pp. 571-574.

[5]. N. Yang, W. K. Henson, J. R. Hauser, and J. J. Wortman, “Estimation of the effects of remote charge scattering on electron mobility of n-MOSFET’s with ultrathin gate oxides,” *IEEE Trans. Electron Devices*, vol. **47**, no. 2, pp. 440-447, Feb. 2000.

[6]. M. V. Fischetti, “Long-range Coulomb interactions in small Si devices Part II. Effective electron mobility in thin-oxide structures,” *J. Appl.Phys.*, vol. **89**, no. 2, pp. 1232–1250, Jan. 2001.

[7]. Z. Ren, M. V. Fischetti, E. P. Gusev, E. A. Cartier, and M. Chudzik, “Inversion channel mobility in high-*k* high performance MOSFETs,” in *IEDM Tech. Dig.*, 2003, pp. 793-796.

[8]. M. V. Fischetti, D. A. Neumayer, and E. A. Cartier, “Effective electron mobility in Si inversion layers in metal-oxide-semiconductor systems with a

high-*k* insulator: The role of remote phonon scattering," *J. Appl. Phys.*, vol. **90**, no. 9, pp. 4587-4608, Nov. 2001.

[9]. R. Chau, S. Datta, M. Doczy, B. Doyle, J. Kavalieros, and M. Metz, "High-*k*/metal-gate stack and its MOSFET characteristics," *IEEE Electron Device Letters*, vol. **25**, no. 6, pp. 408-410, June 2004

[10]. K. H. Cheng, *A Fast Quantum Simulator for the Two-Dimensional Inversion Layers*, *Master Thesis*, National Chiao-Tung University, Sept. 2010.

[11]. D. K. Ferry, *Semiconductors* (Macmillan, New York, 1991)

[12]. J. R. Hauser, "Extraction of experimental mobility data for MOS devices," IEEE Trans. Electron Devices, vol. **43**, no. 11, pp. 1981-1988, Nov. 1996.

[13]. S. Takagi, J. L. Hoyt, J. J. Welser, and J. F. Gibbons, "Comparative study of phonon-limited mobility of two-dimensional electrons in strained and unstrained Si metal-oxide-semiconductor field-effect transistors," *J. Appl. Phys.*, vol. **80**, no. 3, p. 1567, Aug. 1996.

[14]. S. Yamakawa, H. Ueno, K. Taniguchi, C. Hamaguchi, K. Miyatsuji, K. Masaki, and U. Ravaioli, "Study of interface roughness dependence of electron mobility in Si inversion layers using the Monte Carlo method," *J. Appl. Phys.*, vol. **79**, no. 2, pp. 911–916, Jan. 1996.

[15]. Schred. [Online]. Available: http://nanohub.org/resources/schred

[16]. TCAD. http://www.synopsys.com/Tools/TCAD/Pages/default.aspx

[17]. S. Takagi, A. Toriumi, M. Iwase, and H. Tango, "On the universality of inversion layer mobility in Si MOSFETs: Part I—Effects of substrateimpurity concentration," *IEEE Trans. Electron Devices*, vol. **41**, no. 12,276 pp. 2357–2362, Dec. 1994.

[18]. S. Takagi and M. Takayanagi, "Experimental evidence of inversion-layer

mobility lowering in ultrathin gate oxide metal-oxide-semiconductor field-effect-transistors with direct tunneling current," *Jpn. J. Appl. Phys.*, vol. **41**, pt. 1, no. 4B, pp. 2348-2352, Apr. 2002.

[19]. D.W. Lin, M. L. Cheng, S.W.Wang, C. C.Wu, and M. J. Chen, "A novel method of MOSFET series resistance extraction featuring constant mobility criteria and mobility universality," *IEEE Trans. Electron Devices*, vol. **57**, no. 4, pp. 890–897, Apr. 2010.

[20]. K. Romanjek, F. Andrieu, T. Ernst, G. Ghibaudo, "Improved split C-V method for effective mobility extraction in sub-0.1-μm Si MOSFETs" *EDL*, p.583-5, 2004.

[21]. A. Pirovano, A. L. Lacaita, G. Ghidini, and G. Tallarida, "On the correlation between surface roughness and inversion layer mobility in Si-MOSFETs," *IEEE Electron Device Lett.*, vol. **21**, no. 1, pp. 34–36, 367, Jan. 2000.

[22]. W. J. Zhu and T. P. Ma, "Temperature dependence of channel mobility in HfO2-gated NMOSFETs," *IEEE Electron Device Letters*, vol. **25**, no. 2, pp. 89-91, Feb. 2004.

[23]. Q. Xiang, G. Yeap, D. Bang, M. Song, K. Ahmed E. Ibok, and M. R. Lin, "Performance and reliability of sub-100 nm MOSFETswith ultra thin direct tunneling gate oxides," in *VLSI Symp. Tech. Dig.*,Jun. 1998, pp. 160–161.

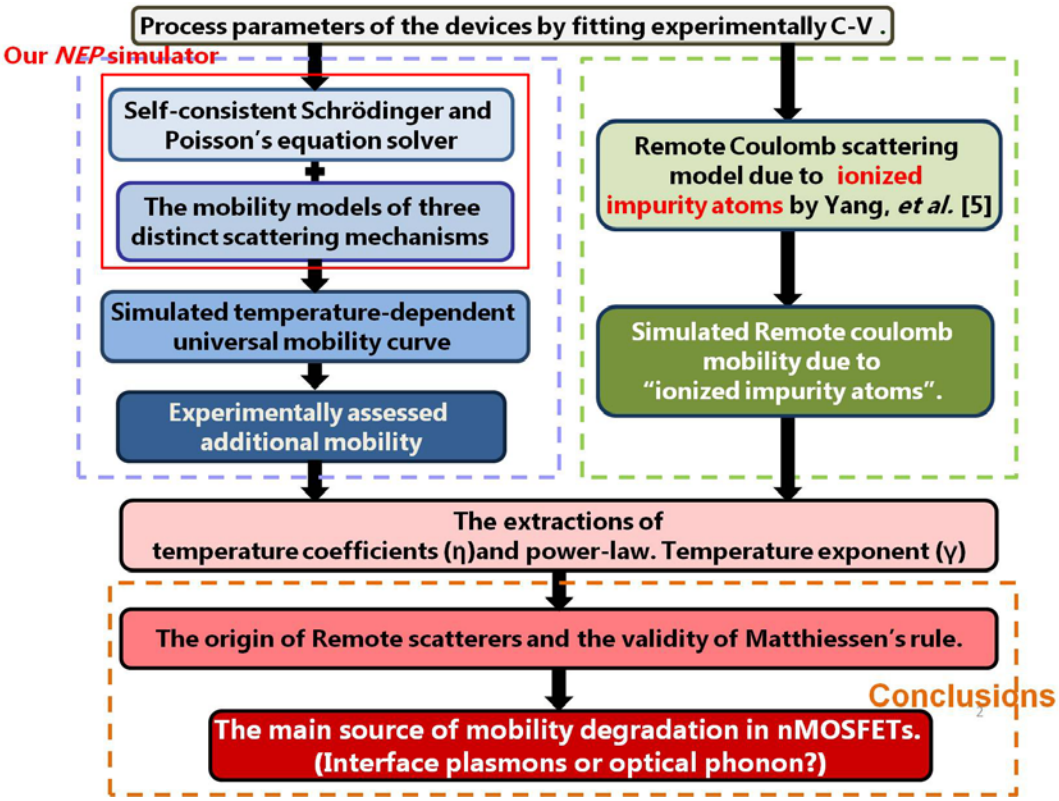

Figure 1.1 The framework of this work in nMOSFETs to distinguish remote scatterers.

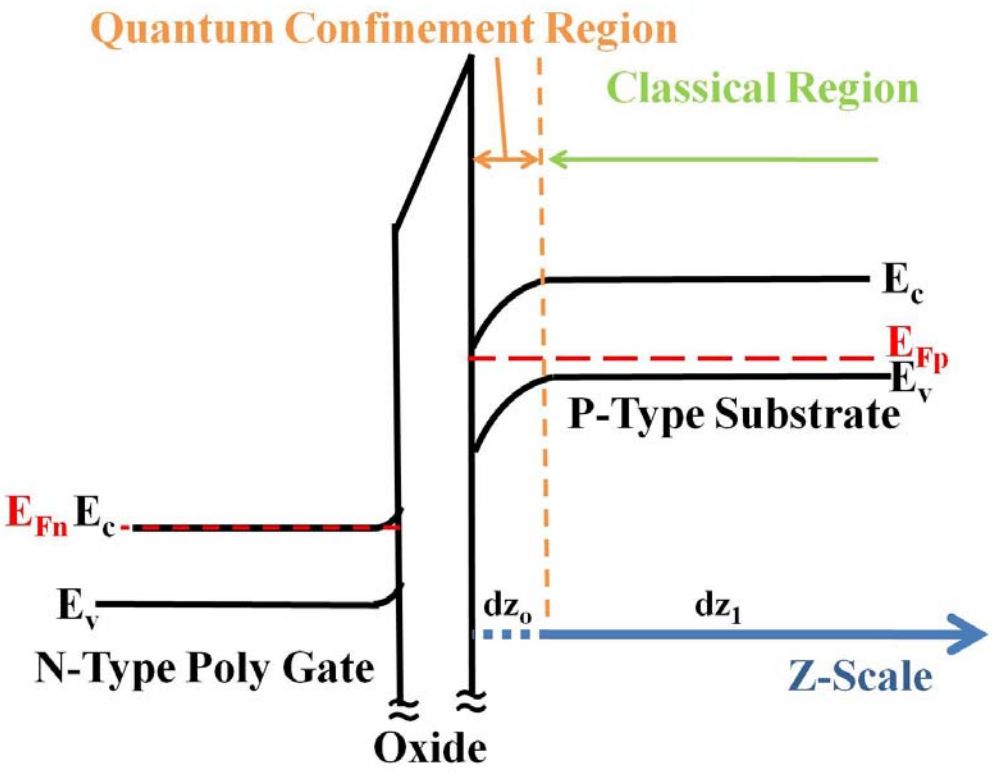

Figure 2.1 The energy band diagram in a poly gate/SiO_2/P-substrate system.

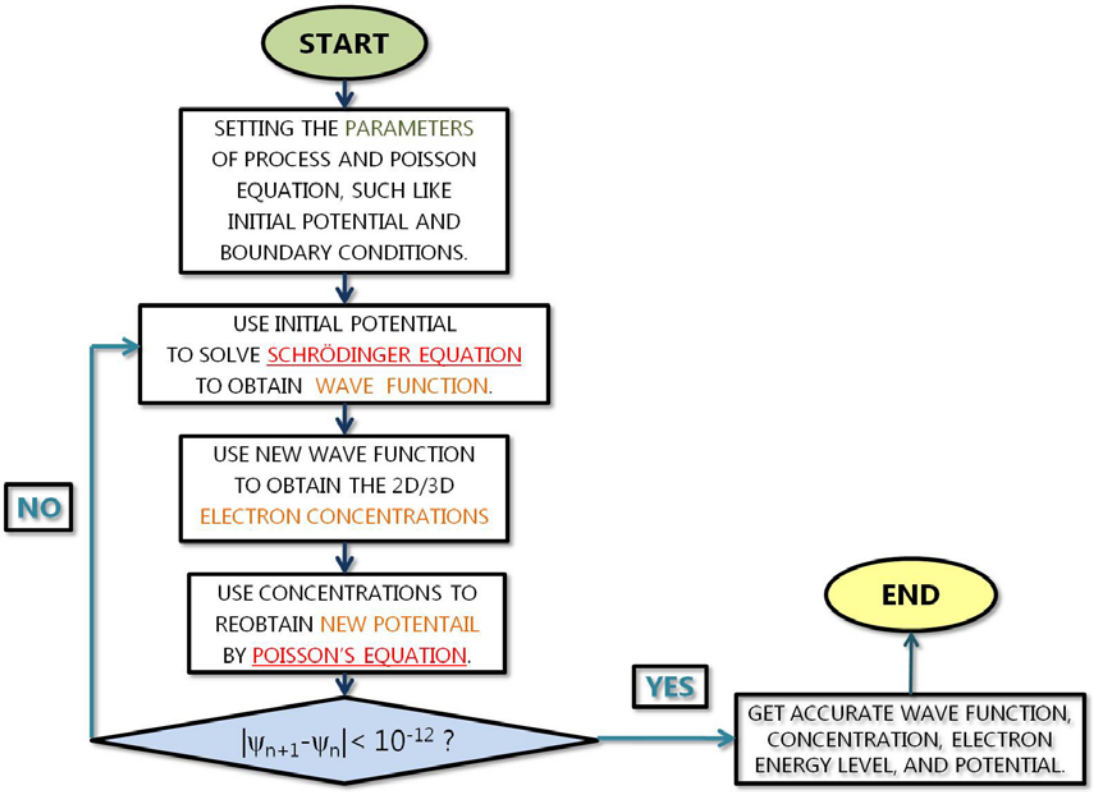

Figure 2.2 The flowchart of Schrödinger and Poisson self-consistent process.

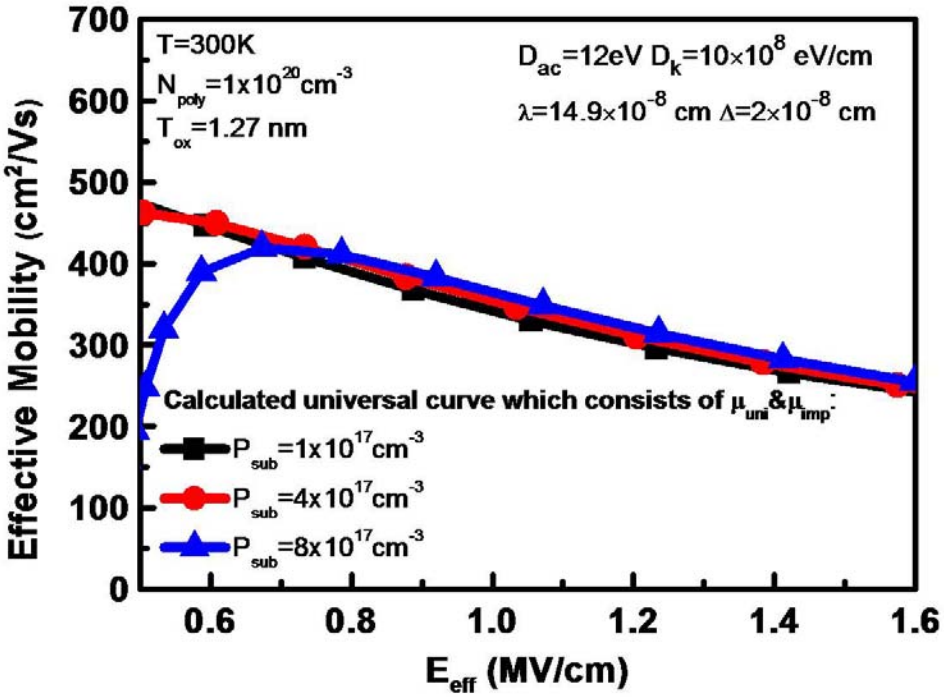

Figure 2.3 The calculated universal mobility (solid lines with symbols) versus vertical effective electric field with substrate doping concentration (P_{sub}) as a parameter.

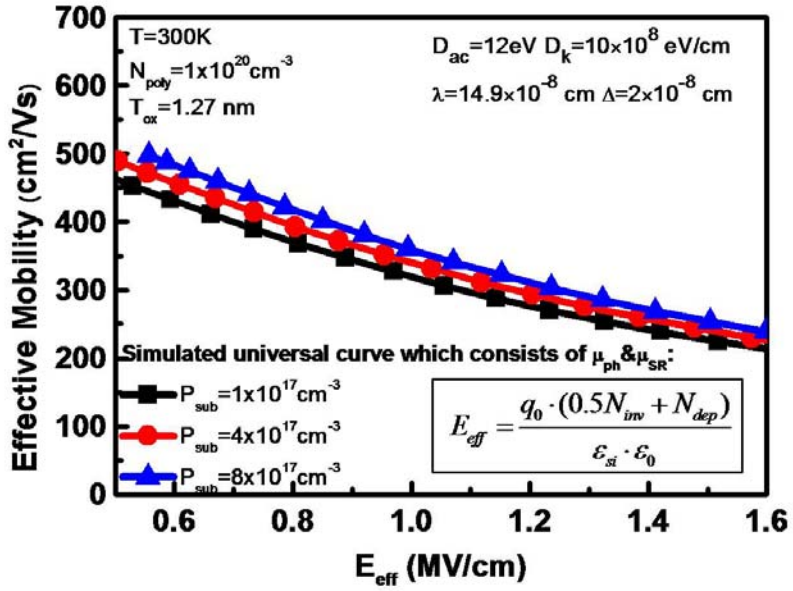

(a)

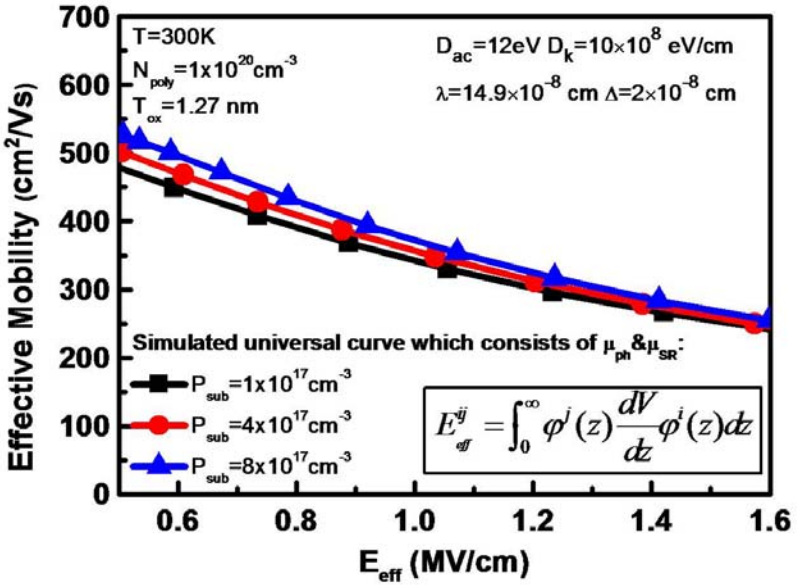

(b)

Figure 2.4 The simulated universal curves (solid lines with symbols) with N_{sub} as a parameter by different definitions of vertical effective electric field in surface roughness's model: (a). The experimentally empirical formula. (b). The definition of vertical electric field in Eq.(2.30) [14].

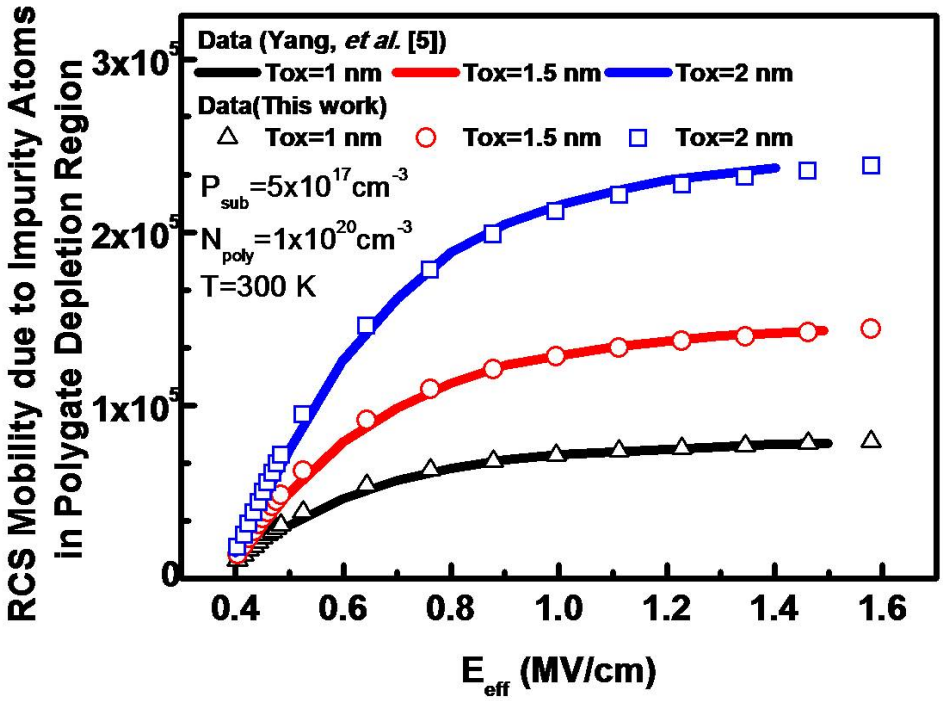

Figure 2.5 The calculated remote Coulomb-limited mobility (symbols) due to ionized impurity atoms in polysilicon depletion region in reproducing simulated data (lines) [5], plotted versus vertical effective electric field for the three oxide thicknesses of 1, 1.5, and 2 nm.

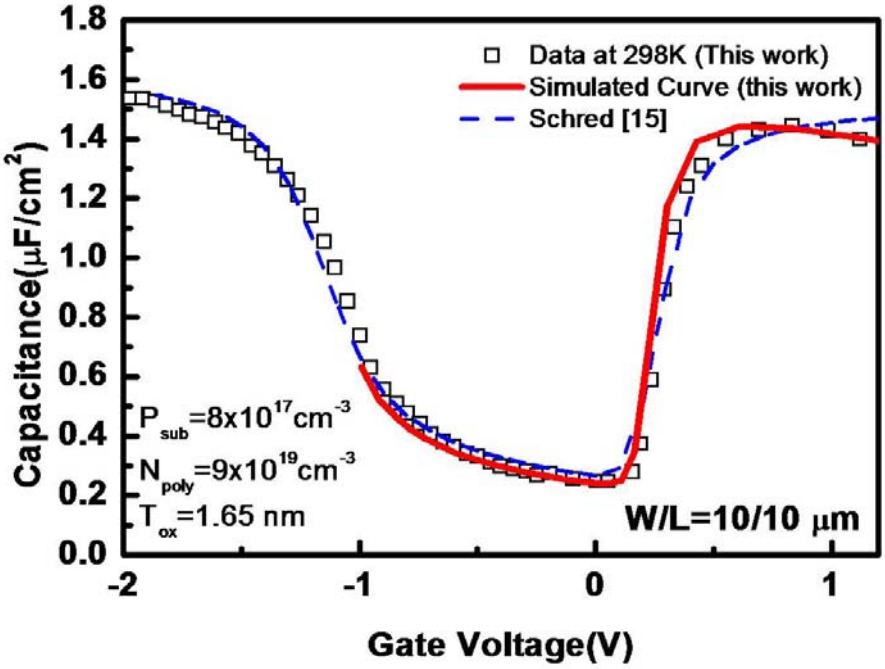

Figure 3.1 The comparison of the measured (symbol) and simulated (lines) gate capacitance versus gate voltage. In addition, the dotted lines came from the self-consistent Schrödinger and Poisson's equations solvers [15].

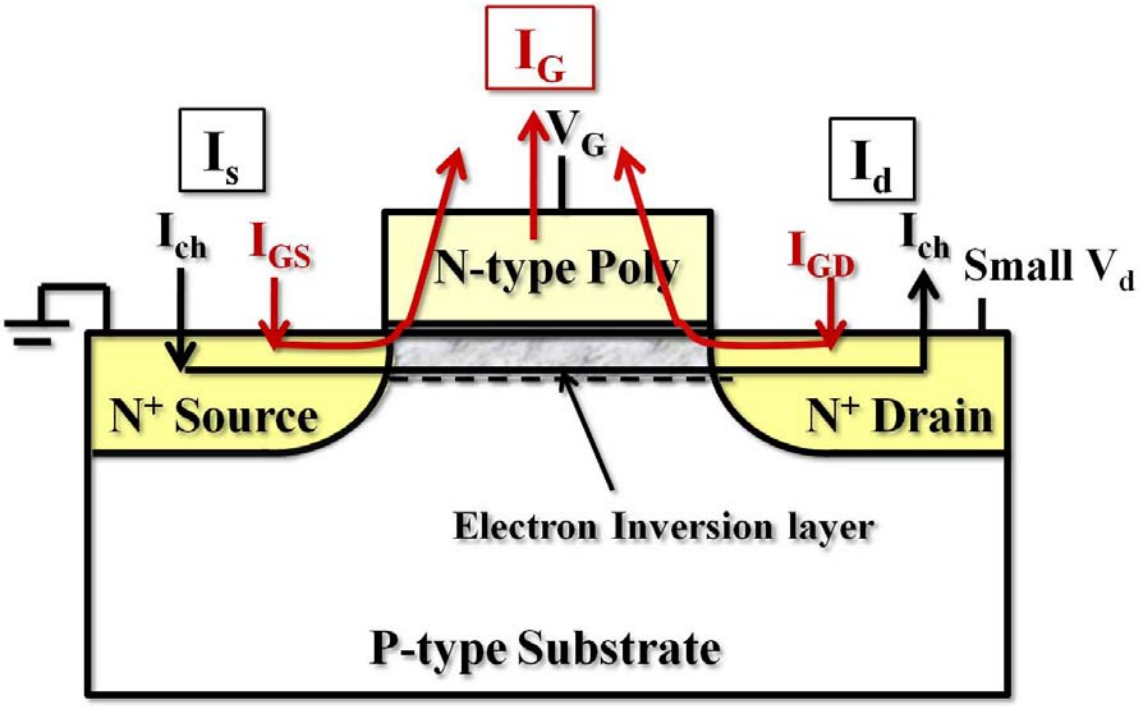

Figure 3.2 The schematic diagram for current flow of nMOSFETs with large gate tunneling current. Besides, $I_S>0$ and $I_d<0$.

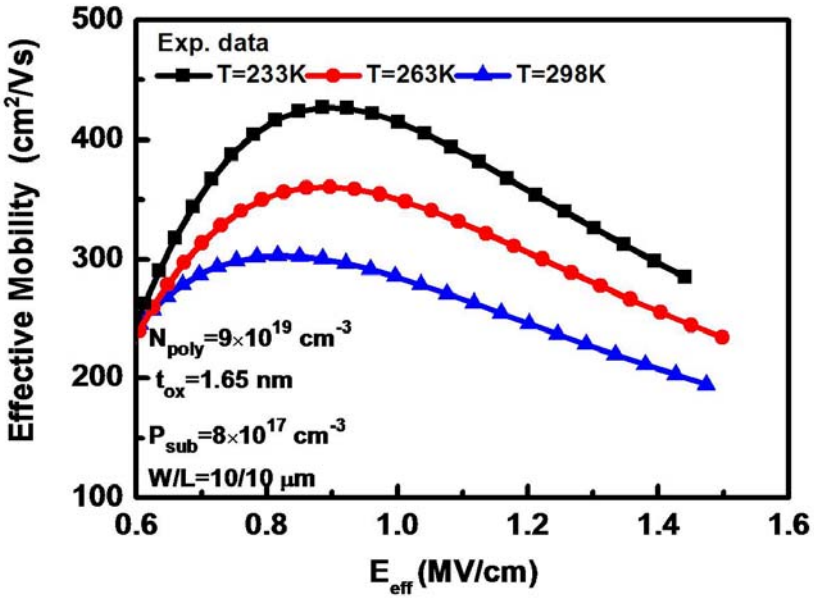

(a)

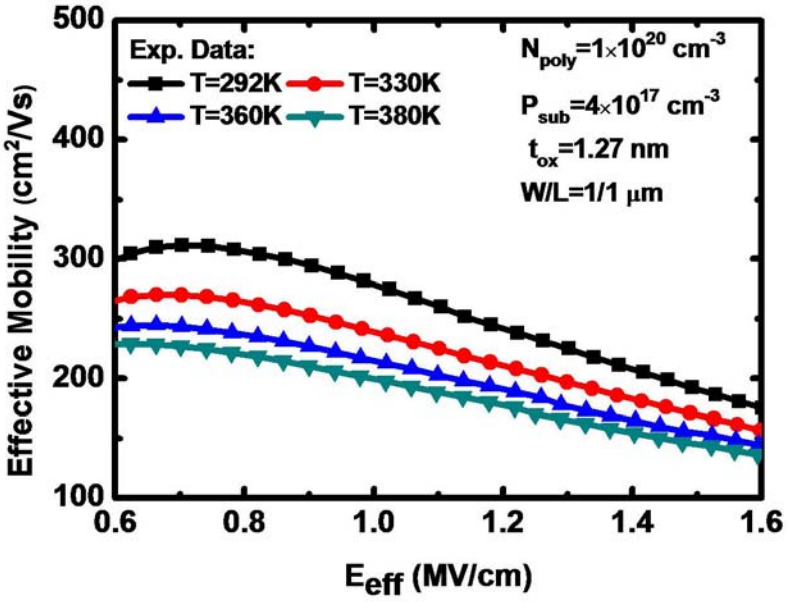

(b)

Figure 3.3 Measured electron effective mobility (Solid lines with symbols) versus vertical effective electric field for (a). W/L=10/10 μm with the three temperatures of 233, 263, 298 K. (b). W/L=1/1μm with four temperatures of 292, 330, 360, and 380 K.

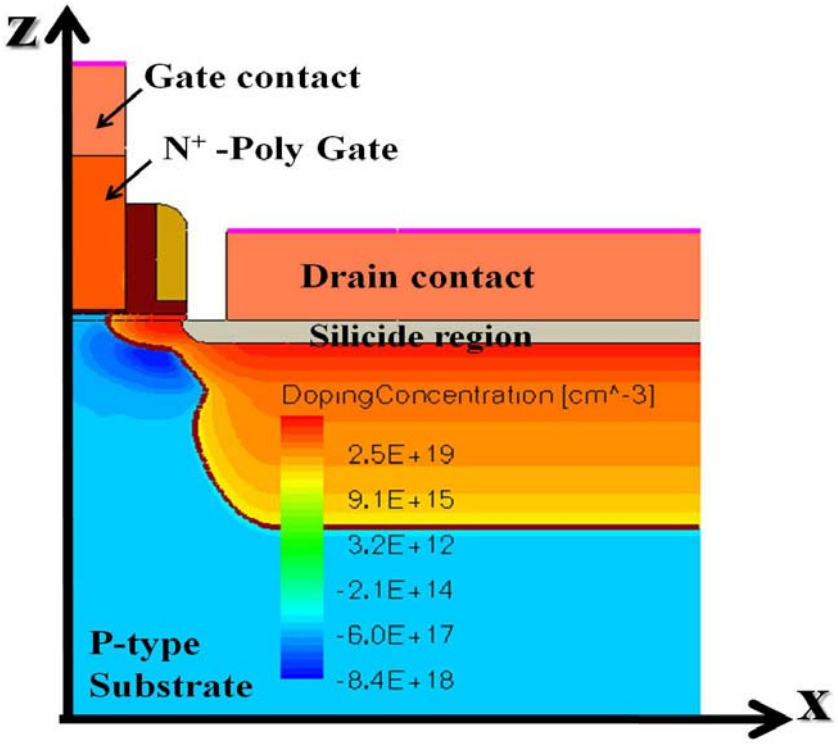

Figure 3.4 The simulated doping profile of nMOSFETs. Here, the blue color represents p-type doping and red color depicts n-type one.

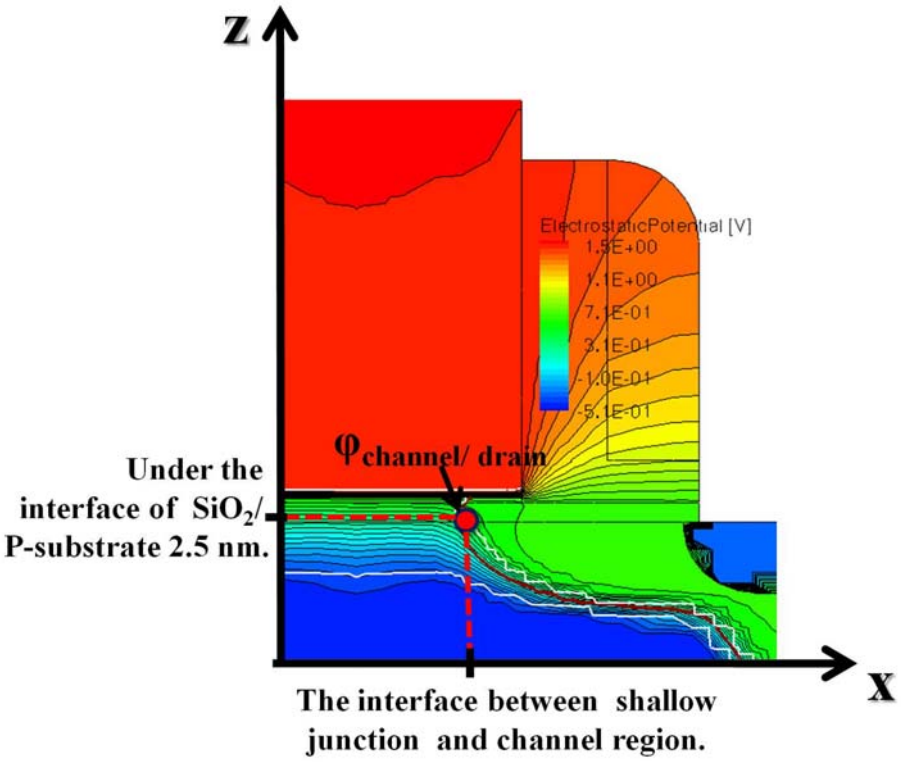

Figure 3.5 The simulated electrostatic potential profile of nMOSFETs. $\varphi_{channel/drain}$ is the potential which locates in the surface between drain extension region and channel region. Its value is extracted below the SiO2/Si substrate interface 2.5 nm.

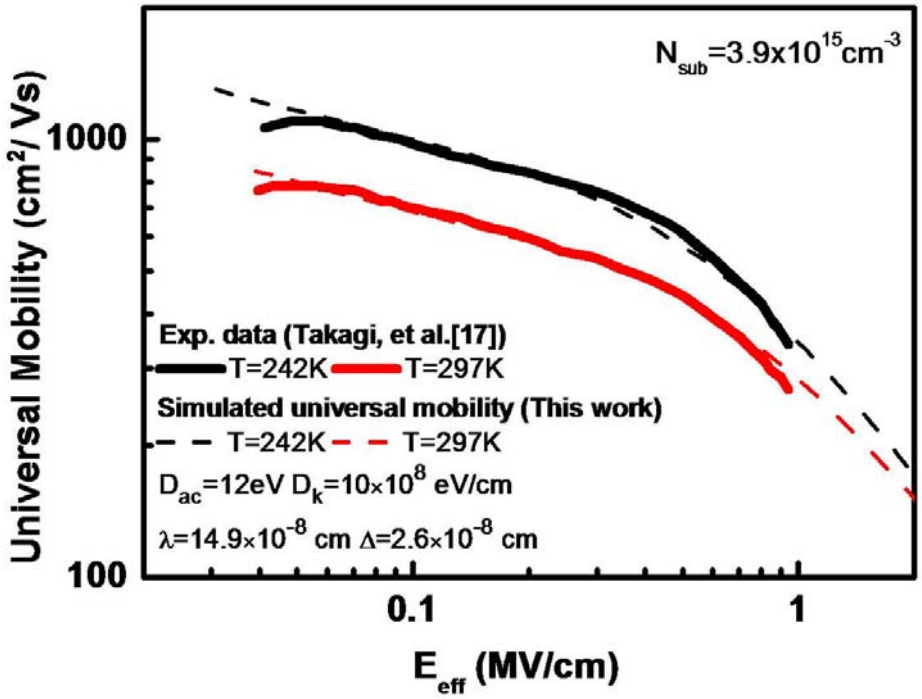

Figure 4.1 Comparison of simulated electron universal mobility curves for two temperatures of 242K and 297K in this work (dotted lines) with the experimental one (solid lines) [17].

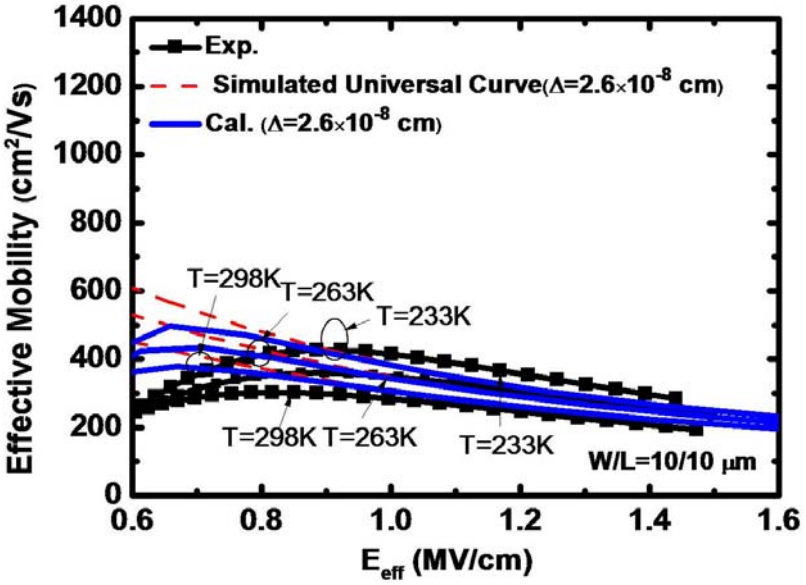

(a)

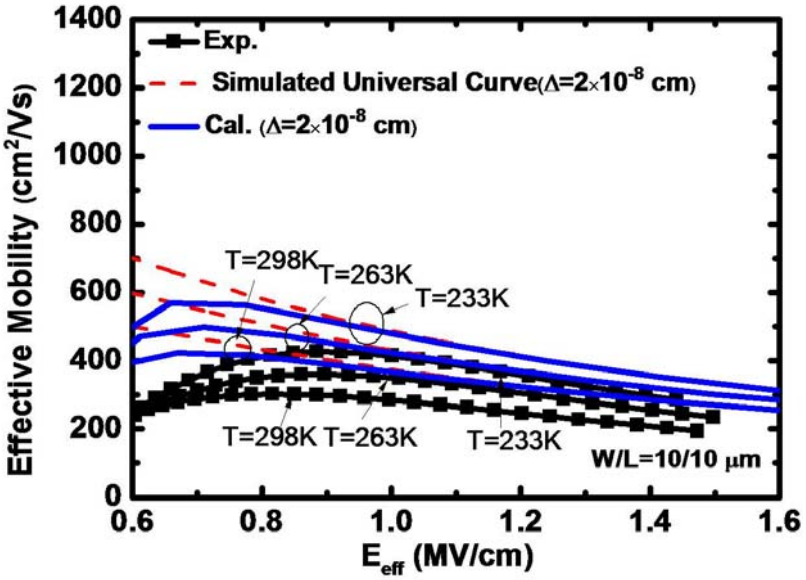

(b)

Figure 4.2 Calculated effective mobility (solid lines), the simulated one (dotted lines), and the measured one (lines with symbols) for three temperatures of 233, 263, and 298 K with W/L=10/10 μm, plotted versus vertical effective electric field for (a) Δ = 2.6 Å, (b) Δ = 2.0 Å, (c) Δ = 1.8 Å, (d) Δ = 1.6 Å, (e) Δ = 1.4 Å, and (f) Δ = 1.2 Å.

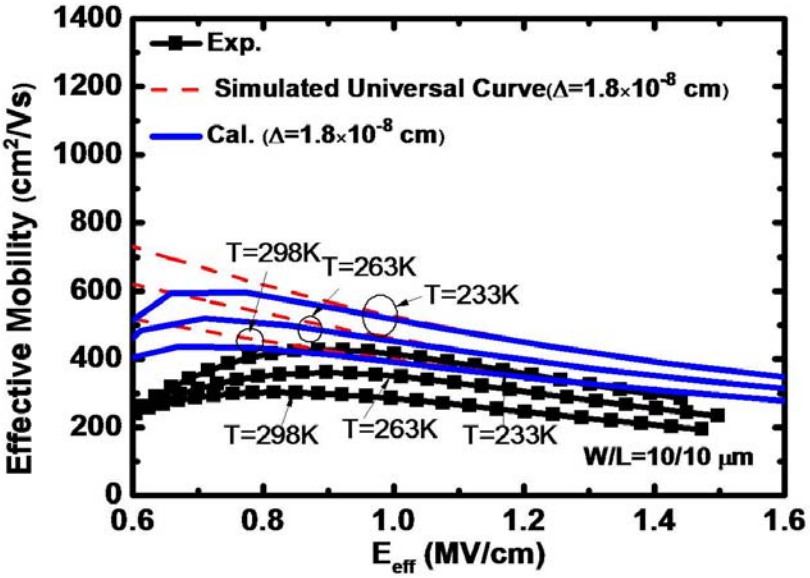

(c)

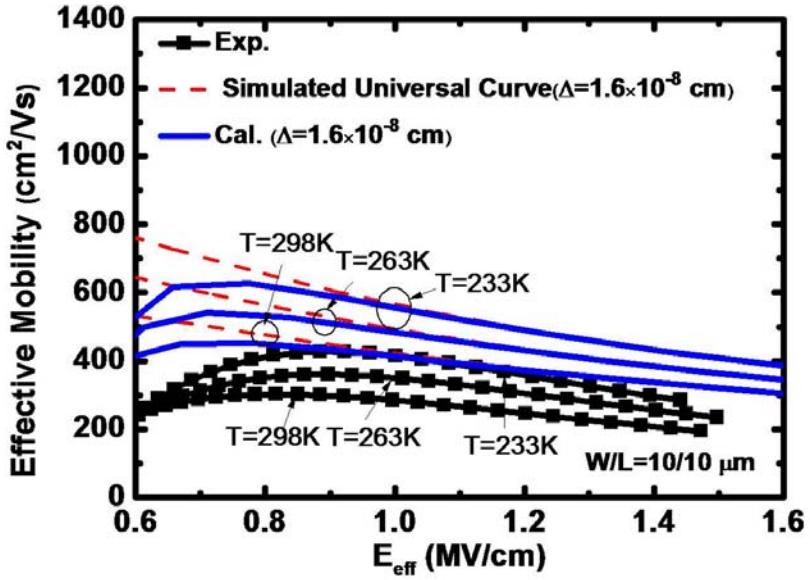

(d)

Figure 4.2 Calculated effective mobility (solid lines), the simulated one (dotted lines), and the measured one (lines with symbols) for three temperatures of 233, 263, and 298 K with W/L=10/10 μm, plotted versus vertical effective electric field for (a) Δ = 2.6 Å, (b) Δ = 2.0 Å, (c) Δ = 1.8 Å, (d) Δ = 1.6 Å, (e) Δ = 1.4 Å, and (f) Δ = 1.2 Å.

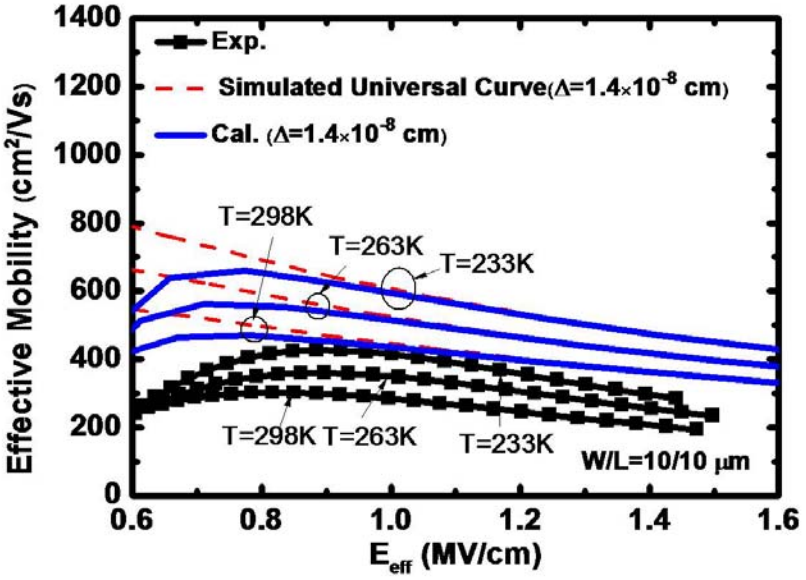

(e)

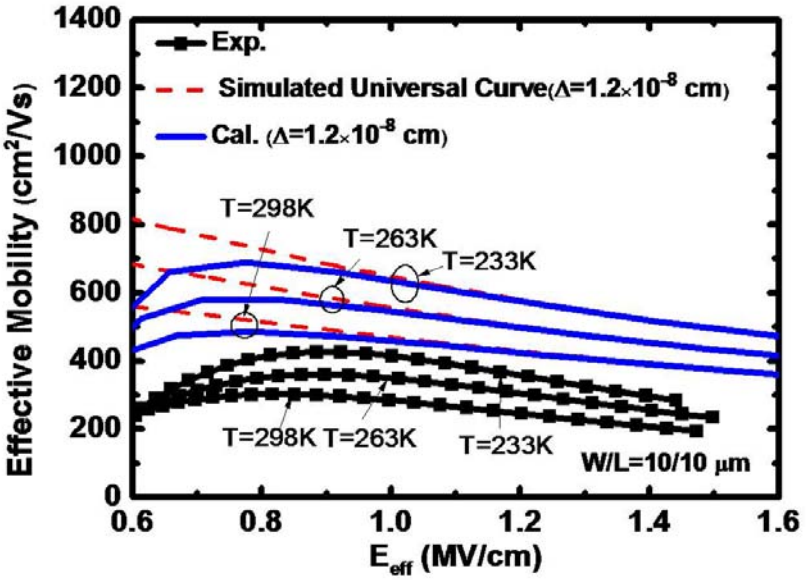

(f)

Figure 4.2 Calculated effective mobility (solid lines), the simulated one (dotted lines), and the measured one (lines with symbols) for three temperatures of 233, 263, and 298 K with W/L=10/10 μm, plotted versus vertical effective electric field for (a) Δ = 2.6 Å, (b) Δ = 2.0 Å, (c) Δ = 1.8 Å, (d) Δ = 1.6 Å, (e) Δ = 1.4 Å, and (f) Δ = 1.2 Å.

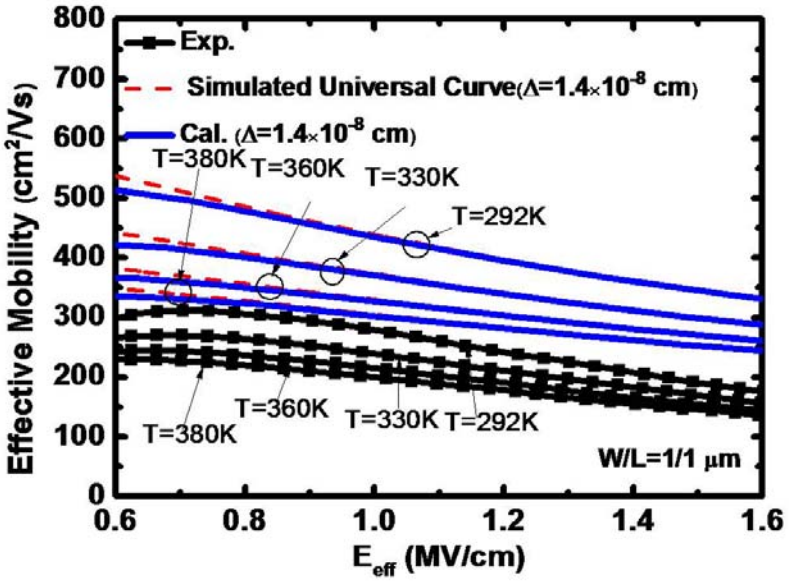

(a)

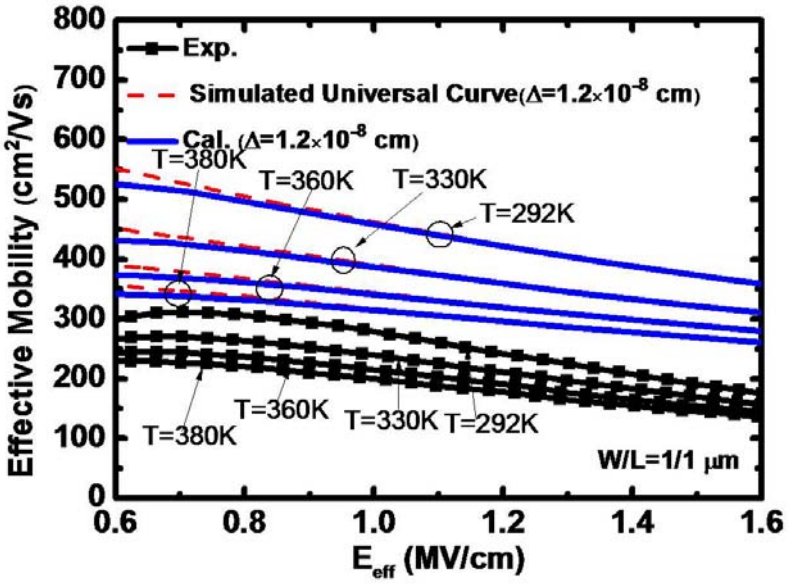

(b)

Figure 4.3 Calculated effective mobility (solid lines), the simulated one (dotted lines), and the measured one (lines with symbols) for four temperatures of 292, 330, 360, and 380 K with W/L=1/1 μm, plotted versus vertical effective electric field for (a) Δ = 1.4 Å, (b) Δ = 1.2 Å, (c) Δ = 1.0 Å, (d) Δ = 0.8 Å.

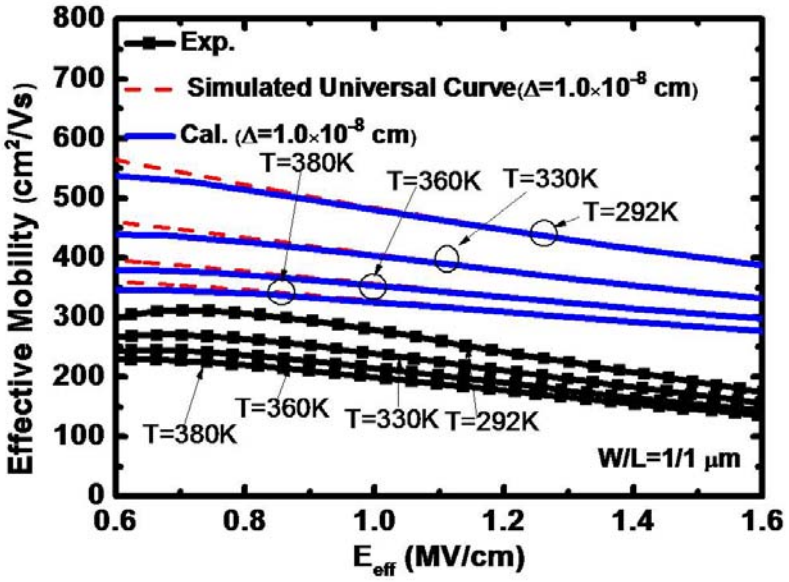

(c)

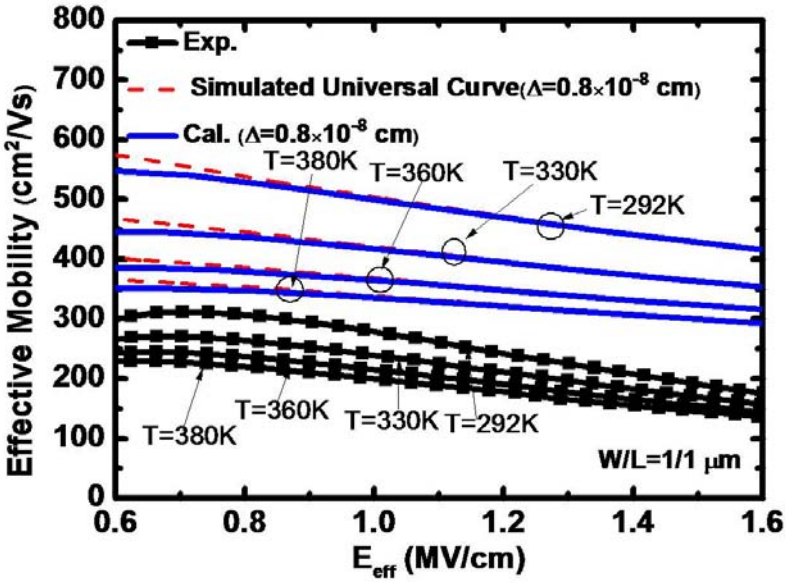

(d)

Figure 4.3 Calculated effective mobility (solid lines), the simulated one (dotted lines), and the measured one (lines with symbols) for four temperatures of 292, 330, 360, and 380 K with W/L=1/1 μm, plotted versus vertical effective electric field for (a) Δ = 1.4 Å, (b) Δ = 1.2 Å, (c) Δ = 1.0 Å, (d) Δ = 0.8 Å.

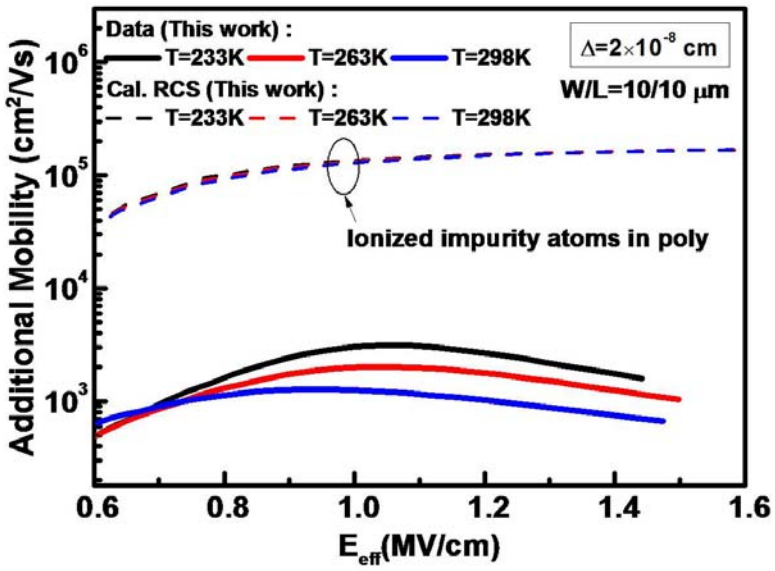

(a)

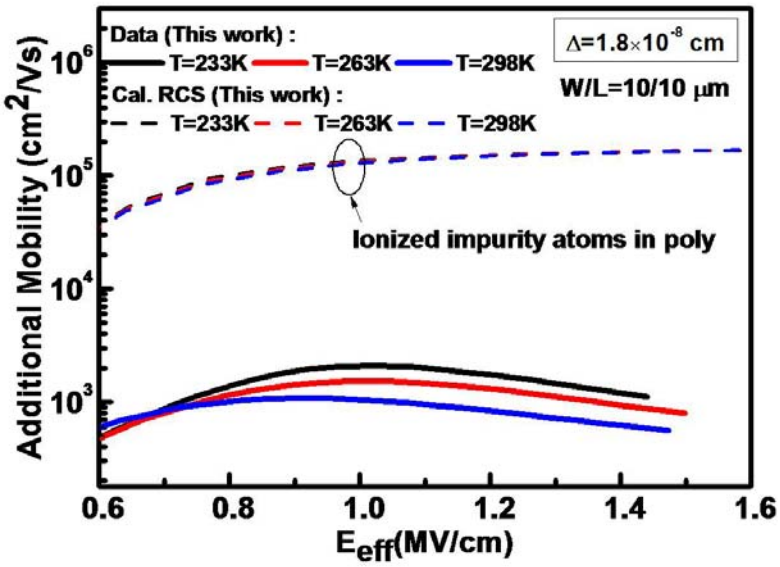

(b)

Figure 4.4 The experimentally assessed additional mobility (solid lines) for three temperatures with W/L=10/10μm, plotted versus vertical effective electric field for (a) Δ = 2.0 Å, (b) Δ = 1.8 Å, (c) Δ = 1.6 Å, (d) Δ = 1.4 Å, and (e) Δ = 1.2 Å. Also shown is the calculated remote Coulomb scattering limited mobility (dotted lines) due to ionized impurity atoms in polysilicon depletion region for three temperatures.

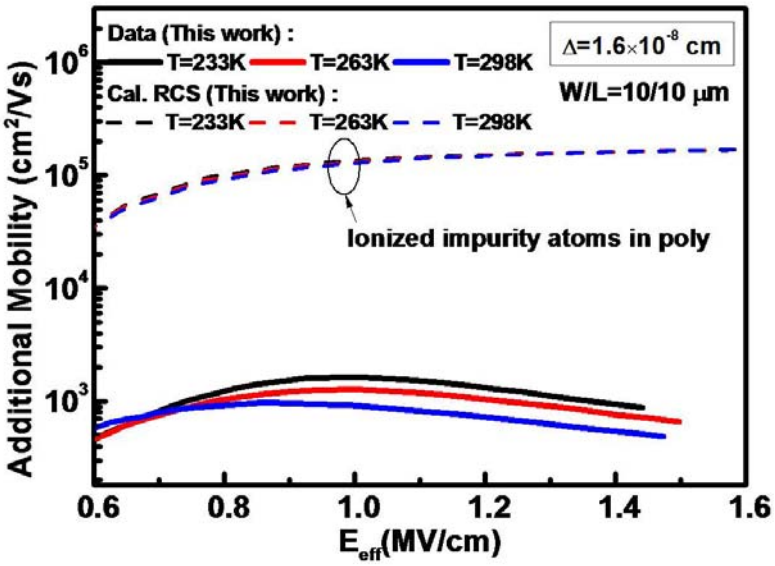

(c)

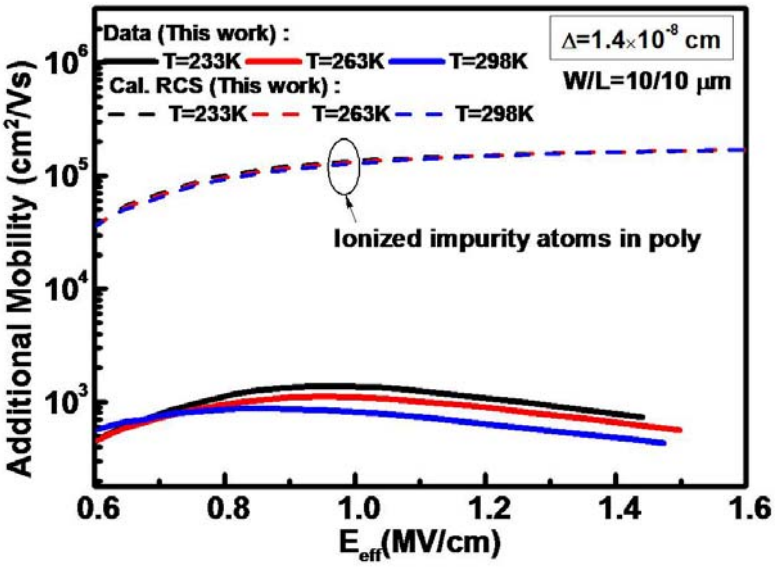

(d)

Figure 4.4 The experimentally assessed additional mobility (solid lines) for three temperatures with W/L=10/10μm, plotted versus vertical effective electric field for (a) Δ = 2.0 Å, (b) Δ = 1.8 Å, (c) Δ = 1.6 Å, (d) Δ = 1.4 Å, and (e) Δ = 1.2 Å. Also shown is the calculated remote Coulomb scattering limited mobility (dotted lines) due to ionized impurity atoms in polysilicon depletion region for three temperatures.

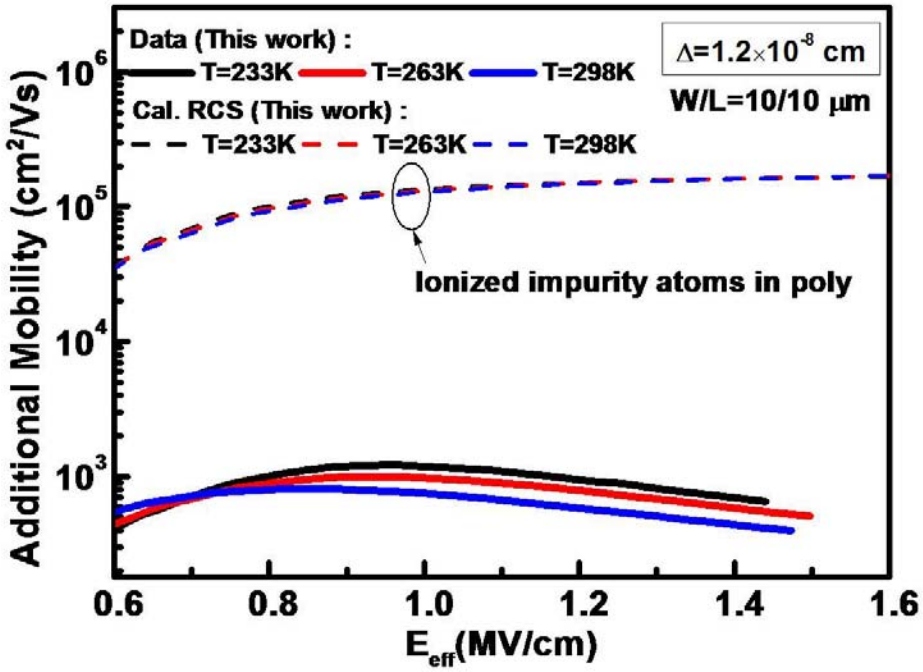

(e)

Figure 4.4 The experimentally assessed additional mobility (solid lines) for three temperatures with W/L=10/10μm, plotted versus vertical effective electric field for (a) Δ = 2.0 Å, (b) Δ = 1.8 Å, (c) Δ = 1.6 Å, (d) Δ = 1.4 Å, and (e) Δ = 1.2 Å. Also shown is the calculated remote Coulomb scattering limited mobility (dotted lines) due to ionized impurity atoms in polysilicon depletion region for three temperatures.

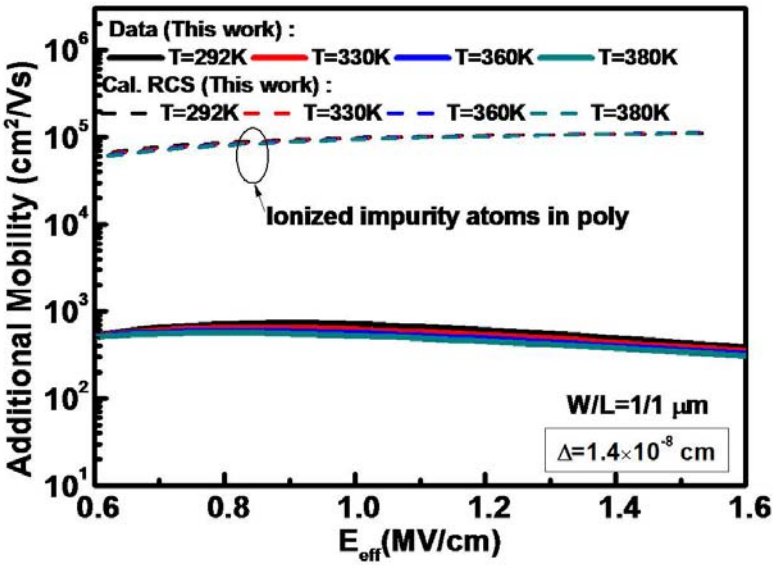

(a)

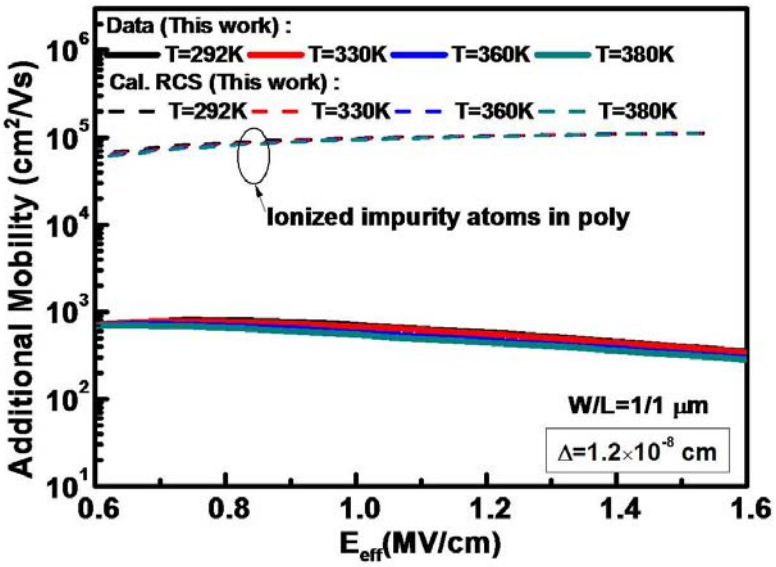

(b)

Figure 4.5 The experimentally assessed additional mobility (solid lines) for four temperatures with W/L=1/1μm, plotted versus vertical effective electric field for (a) Δ = 1.4 Å, (b) Δ = 1.2 Å, (c) Δ = 1.0 Å, and (d) Δ = 0.8 Å. Also shown is the calculated remote Coulomb scattering limited mobility (dotted lines) due to ionized impurity atoms in polysilicon depletion region for four temperatures.

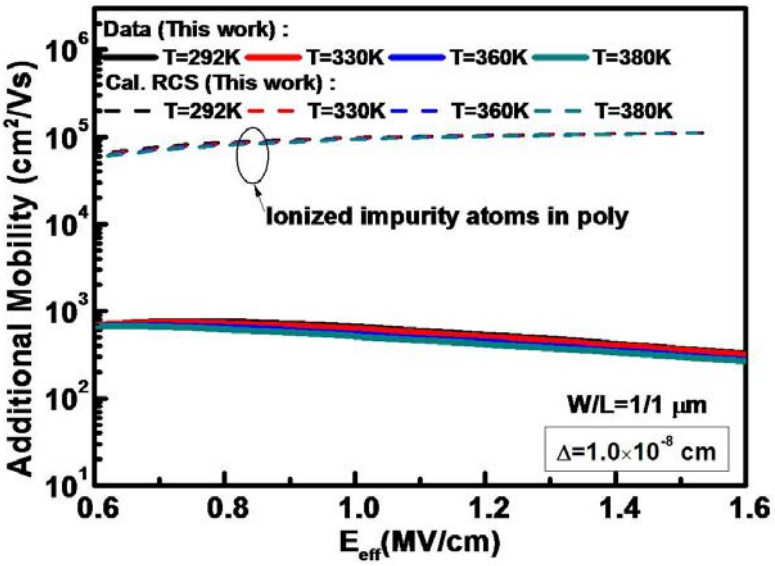

(c)

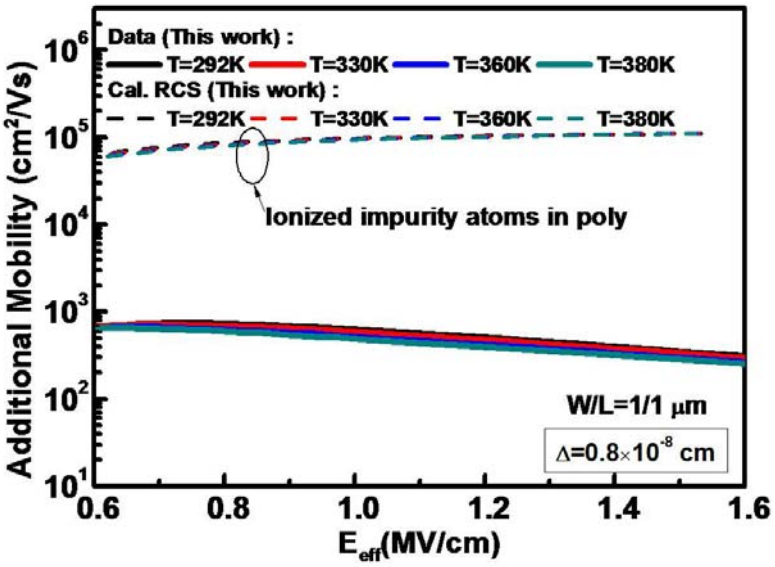

(d)

Figure 4.5 The experimentally assessed additional mobility (solid lines) for four temperatures with W/L=1/1μm, plotted versus vertical effective electric field for (a) Δ = 1.4 Å, (b) Δ = 1.2 Å, (c) Δ = 1.0 Å, and (d) Δ = 0.8 Å. Also shown is the calculated remote Coulomb scattering limited mobility (dotted lines) due to ionized impurity atoms in polysilicon depletion region for four temperatures.

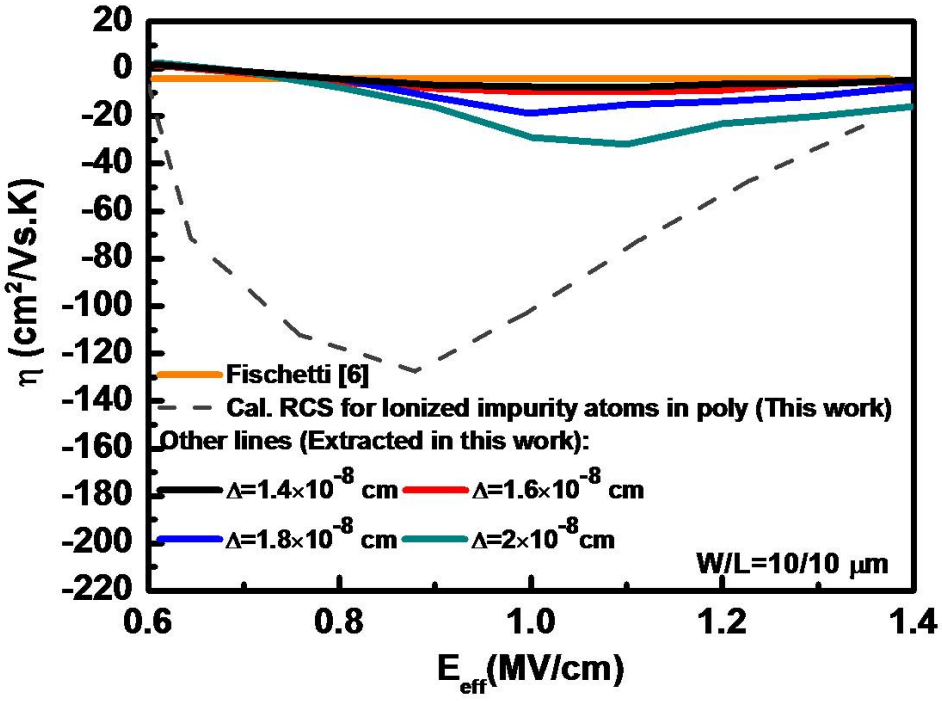

Figure 4.6 Temperature coefficients of extracting experimentally additional mobility (solid lines) in this work, along with those of the calculated remote Coulomb scattering (RCS) limited mobility (dotted lines) due to ionized impurity atoms in polysilicon depletion region. Also represented is the possible range where the simulated temperature coefficient [6] yielded a value of - 4.15 cm^2/VsK.

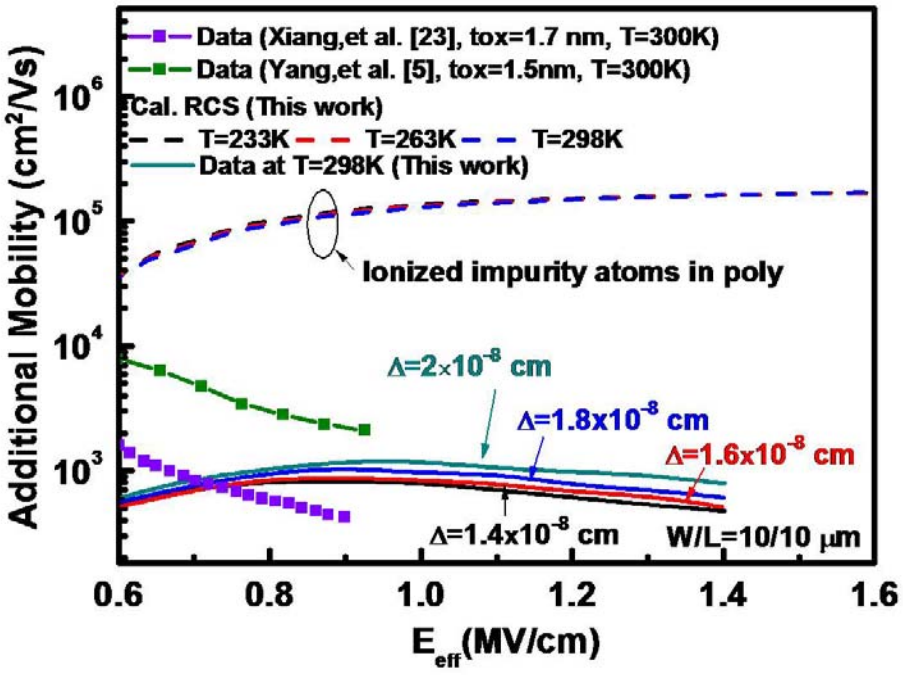

Figure 4.7 Comparison of the experimentally assessed additional mobility (solid lines) near room temperature versus vertical effective electric field with the published [5] and [23] (lines with symbols). Also shown is the calculated remote Coulomb limited mobility (dotted lines) due to the ionized impurity atoms in polysilicon depletion region for three different temperatures.

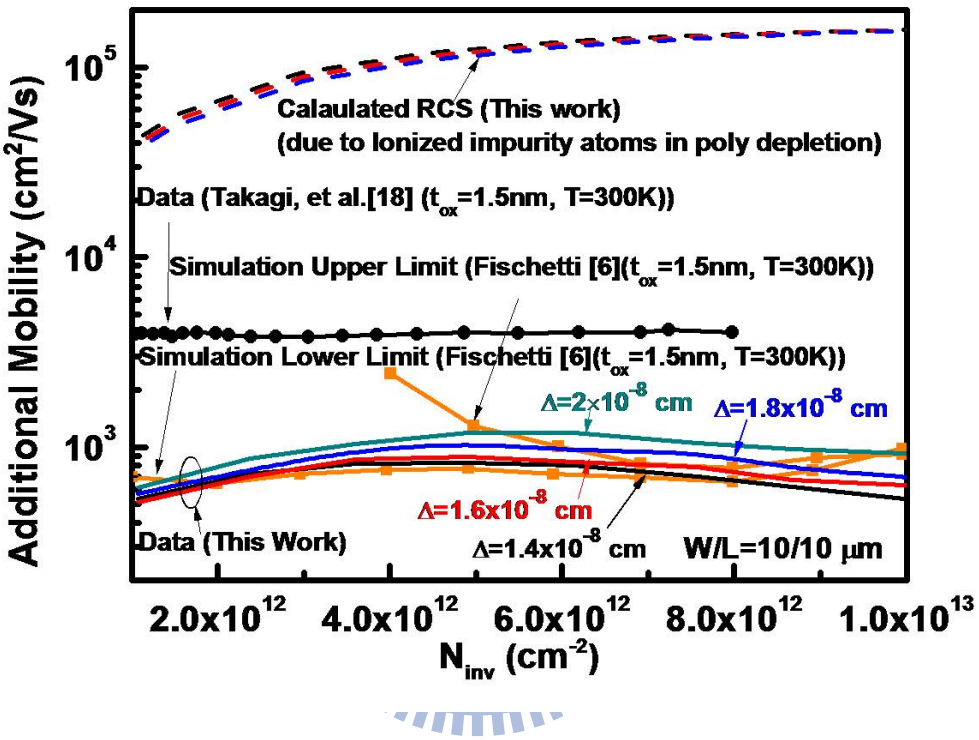

Figure 4.8 Comparison of the experimentally extracted additional mobility (solid lines) near room temperature versus inversion-layer electron sheet density (N_{inv}), with the simulated remote Coulomb limited mobility (lines with squares) due to the interface plasmons in poly side [6], the experimentally extracted additional mobility (line with circle) from [18], and the calculated remote Coulomb scattering (RCS) limited mobility (dotted lines for three different temperatures) due to the ionized impurity atoms in polysilicon depletion region.

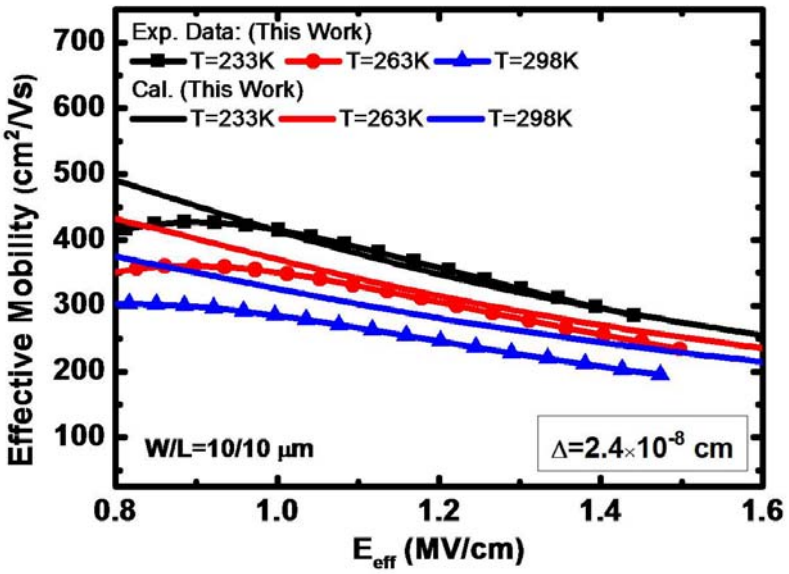

(a)

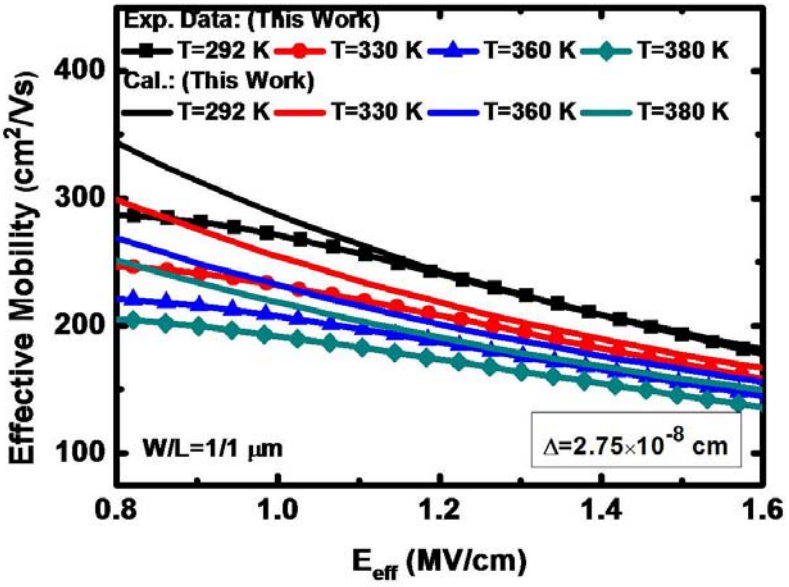

(b)

Figure 4.9 Calculated universal mobility curves with surface roughness amplitude (Δ) as a parameter, along with experimentally extracted mobility for temperature dependent comparison in (a). W/L=10/10 μm and (b).W/L=1/1μm.

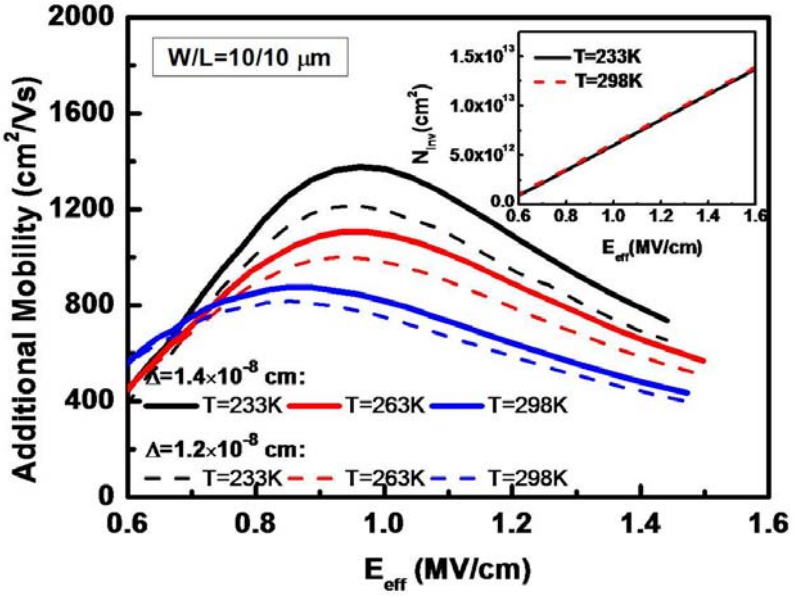

(a)

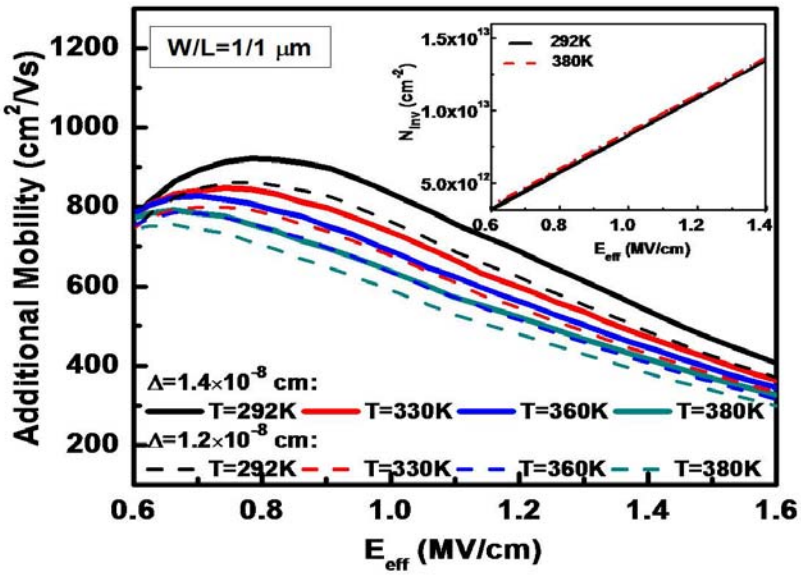

(b)

Figure 4.10 Experimentally extracted additional mobility versus vertical effective field with Δ = 1.2 and 1.4 Å in (a). W/L=10/10 μm for three different temperatures, and (b).W/L=1/1μm for four temperatures. The inset shows simulated inversion-layer density as a function of vertical effective field for two temperatures.

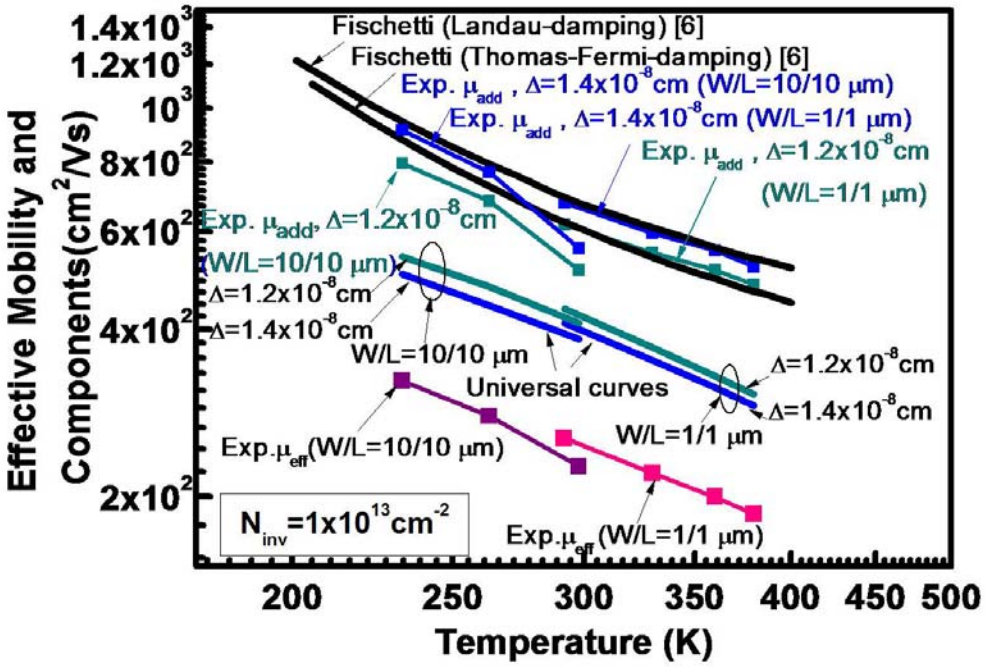

Figure 4.11 The experimental effective mobility, simulated universal mobility, and corresponding additional one, plotted versus temperature for W/L=10/10 μm and 1/1μm at fixed inversion-layer density of 1×10^{13} cm^{-2} in order to make an accurate comparison with simulated interface plasmons limited mobility [6].

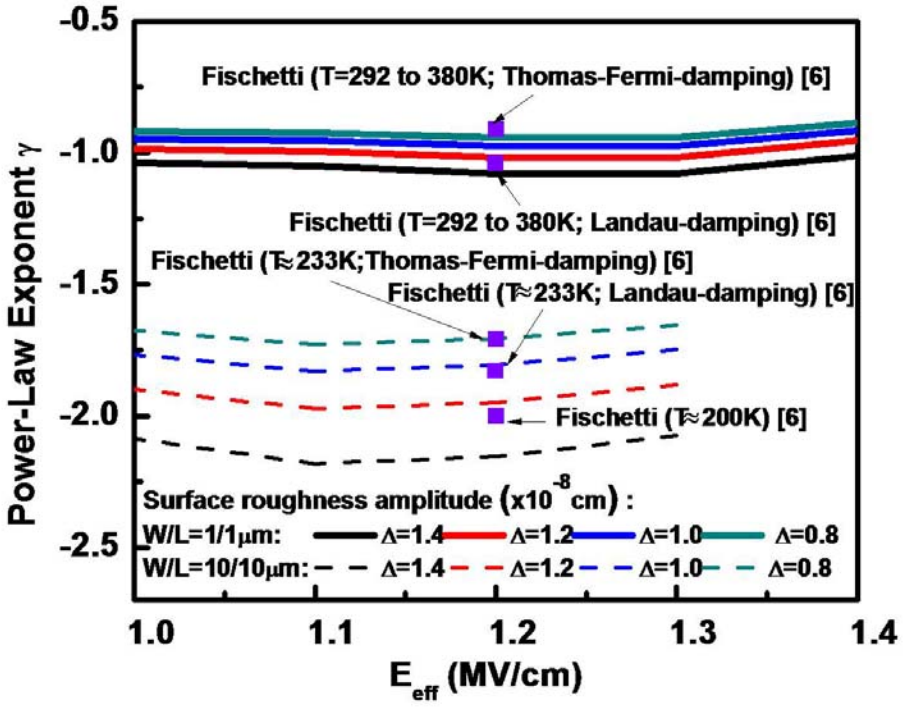

Figure 4.12 Fitted temperature power-law exponent with W/L=10/10 μm (dashed lines) and W/L=1/1 μm (solid lines) versus vertical effective field for four surface roughness amplitudes. Also shown are those from the simulated published (points) [6].

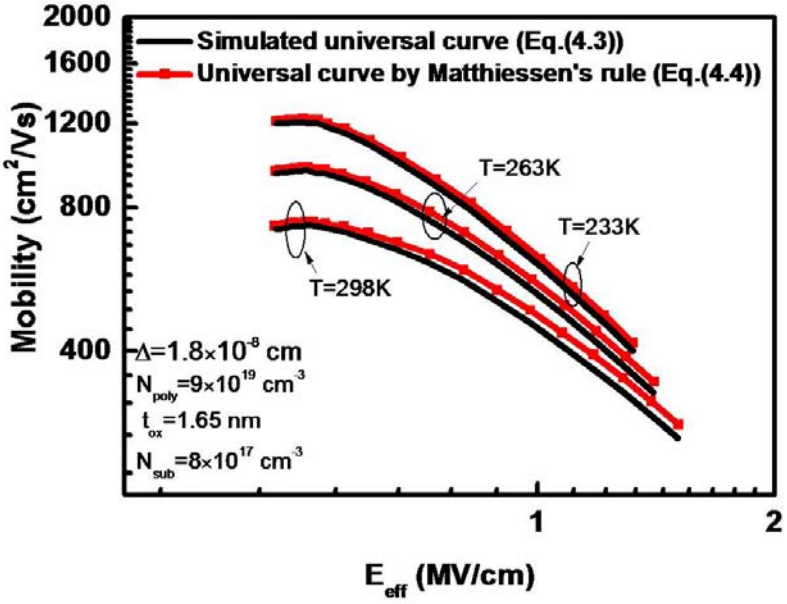

(a)

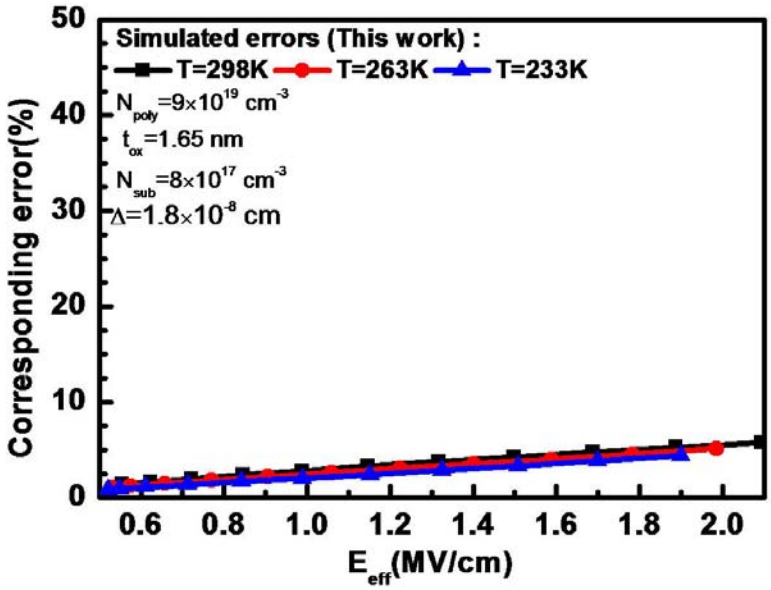

(b)

Figure 4.13 (a) Comparison of the simulated universal mobility from two different calculation methods between Eq. (4.3) and Eq. (4.4), plotted as a function of vertical effective electric field for three temperatures; and (b) the corresponding errors.

Electron Scattering and Physical Parameters for Si					
	This Work	Ferry [11]	Takagi [12]	A. Pirovano [21]	W. J. Zhu [22]
Acoustic Phonon D_{ac} (eV)	12		12		
Optical Phonon for k_{th} Intervalley D_k ($\times 10^8$ eV/cm)	10	7 - 10	19.2		
Crystal Density ρ (kg/cm^3)	2329		2329		
Sound Velocity S_l (m/s)	9037		9037		
Surface Roughness Amplitude Δ ($\times 10^{-8}$ cm)	0.8 - 2		2.6	1.6 - 2.5	1.2
The Correlation Length of Surface Roughness λ ($\times 10^{-8}$ cm)	14.9		14.9	10 - 20	

Table I Electron scattering and physical parameters for Si used in this work as comparison with the values in recently published.

Process Parameters of the Devices		
	W/L=10/10 μm	W/L=1/1 μm
Oxide Thickness T_{ox} (nm)	1.65	1.27
P-type Substrate Doping Concentration P_{sub} (cm^{-3})	$8x10^{17}$ cm^{-3}	$4x10^{17}$ cm^{-3}
N-type Polysilicon Doping Concentration N_{poly} (cm^{-3})	$9x10^{19}$ cm^{-3}	$1x10^{20}$ cm^{-3}
Temperature (K)	233, 263, 298	292, 330, 360, 380
R_{sd} (Ω/μm)	no	117

Table II Process parameters of the devices for nMOSFETs used in this work.

Parasitic Source/ Drain Resistances (Ω/μm)			
Temperature (K)	V_g=0.8 V	V_g=1.0 V	V_g=1.2 V
292 K	124	105	99
330 K	125	106	98
360 K	126	106	99
380 K	127	108	100

Table III The extracted parasitic source/ drain resistances for four temperatures with Vg=0.8, 1.0, and 1.2 V by TCAD simulator [16].